# Autophagy inhibition mediated via an injectable and NO-releasing hydrogel for amplifying the antitumor efficacy of mild magnetic hyperthermia

Yaoben Wang, Xiaobin Chen, Zhiyong Chen, Xin Wang, Hancheng Wang, Huajuan Zhai, Jiandong Ding, Lin Yu[*]

*State Key Laboratory of Molecular Engineering of Polymers, Department of Macromolecular Science, Shanghai Stomatological Hospital & School of Stomatology, Fudan University, Shanghai, 200438, China*

## ABSTRACT

While mild hyperthermia holds great potential in the treatment of solid tumors, the thermal stress-triggered self-repairing autophagy significantly compromises its efficacy. To circumvent this obstacle, an injectable hydrogel (NO-Gel) composed of thermosensitive poly(ethylene glycol)-polypeptide copolymers modified with abundant NO donors on their side chains is developed. Meanwhile, ferrimagnetic $Zn_{0.5}Fe_{2.5}O_4$ magnetic nanoparticles (MNPs) with high magnetic-heat conversion efficiency are synthesized and loaded into NO-Gel to obtain MNPs@NO-Gel. The MNPs@NO-Gel system exhibits a sol-gel transition upon heating, and has the ability to perform multiple magnetic hyperthermia therapy (MHT) after only one administration due to the even distribution and strong immobilization of MNPs in NO-Gel. NO can be continuously liberated from NO-Gel and this process is markedly accelerated by MHT. Additionally, MNPs@NO-Gel maintains its integrity *in vivo* for over one month and the released MNPs are metabolized by the spleen. After a single administration of MNPs@NO-Gel at the tumor site, three mild MHT treatments with similar effects are fulfilled, and the sufficient supply of NO effectively inhibits MHT-induced autophagic flux *via* blocking the formation of autophagosomes and synchronously destroying lysosomes, thereby substantially boosting the efficacy of mild MHT. As a consequence, CT-26 colon tumors are completely eliminated without causing severe side-effects.

## 1. Introduction

Hyperthermia can kill tumor cells by damaging organelles such as mitochondria and denaturing proteins [1,2]. From 2500 BCE to the 19th century, many efforts had been made to utilize heat to ablate tumors, such as burning tumors directly or making patients feverish [2]. However, these ways invariably harm normal organs and tissues. With advances in nanotechnology, great progress has been made in nanoparticles-mediated hyperthermia, which can absorb energy stemmed from various external sources such as laser, microwave, alternating magnetic field (AMF), radiofrequency and ultrasound to precisely induce thermal destruction of tumors [3–5]. Thereinto, magnetic hyperthermia therapy (MHT) is an emerging non-invasive therapeutic strategy that utilizes magnetic-to-thermal conversion of magnetic nanoparticles (MNPs) under an external AMF to achieve the treatment of solid tumors [4,6–8]. Owing to the trait of unlimited penetration depth,

MHT has received extensive attention in clinic [4,6,9–12]. For example, NanoTherm® manufactured by Magforce company is a kind of $Fe_3O_4$ superparamagnetic nanoparticles coated with aminosilane. In 2011, MHT mediated by NanoTherm® was approved by the European Union as an adjuvant to glioblastoma radiotherapy, and the combination treatment significantly prolonged the median survival time of patients [9].

Usually, there are two temperature windows in tumor hyperthermia [2]. When the temperature of the tumor region is above 50 °C, it is called thermal ablation, which can completely eliminate the tumor, but inevitably injures adjacent tissues or organs and brings unendurable heat-induced pains to patients [7,13–15]. Mild hyperthermia in another window (41–46 °C) is a more favorable approach to tumor treatment, which can reduce damage to neighboring tissues or organs [7,10,13]. However, the damage caused by mild hyperthermia to tumors is often recoverable due to the self-protecting mechanism of tumor cells [7,14,

---

16]. Autophagy is an important self-repairing pathway of cells [17]. In detail, phagophores with a double membrane structure can engulf damaged proteins, organelles and other components to form autophagosomes. Next, autophagosomes are transformed into autolysosomes by fusing with lysosomes. After that, these encapsulated components are degraded *via* enzymes carried by lysosomes into amino acids, acetyl-CoA, pyruvate, etc [7]. Finally, these nutrients are recycled to renew cells. When tumor cells suffer from cellular stresses, especially heat stress, autophagy will be activated to repair the damaged cells, resulting in thermal resistance of tumors [7,18,19].

Nitric oxide (NO), a vital endogenous gas messenger, is involved in multifarious physiological functions, like angiogenesis [20–22], vasodilation [22,23], immunoregulation [24], and so on [25,26]. NO also exhibits antitumor activity at high concentrations [27]. Moreover, it has been reported that NO can impair autophagy in the early stage of autophagosome formation by inhibiting the JNK1-Bcl-2-Beclin1 pathway and activating mTORC1 [28]. Some studies have utilized exogenous NO to suppress autophagic flux, thereby improving the antitumor efficacy of various therapies [13,29,30]. Nonetheless, owing to its high activity and short half-life, exogenous NO is quickly cleared by the circulatory system before it reaches the target site. Therefore, achieving sustained and adequate delivery of NO at the tumor site remains a great challenge.

To date, a variety of nano-delivery systems modified or loaded with NO donors have been exploited [24,31–36]. However, these systems suffer from the low efficiency of donor loading and NO leakage in the blood circulation, which seriously affect the amount of NO targeted to tumors [23,37]. Different from systemic administration, local delivery offers an attractive alternative that can not only increase NO supply to tumors, but also reduce NO distribution at non-tumor sites.

Injectable hydrogels are suitable as topical delivery carriers and tissue repair scaffolds [38–42]. In particular, various thermo-induced gelation systems composed of poly(ethylene glycol) (PEG)-polyester copolymers [43–48], PEG-polypeptide copolymers [40,49–53], and poly (organophosphazene) [54–56] have been developed for local drug delivery and other biomedical applications. Usually, these systems exhibit injectable sols at room or low temperatures and spontaneously transform into non-flowing physical hydrogels at physiological temperature [38,49]. Hence, therapeutic agents or MNPs can be easily encapsulated *via* simply mixing in the sol state. After injection at the lesion site, the mixtures rapidly transform into *in situ* hydrogel reservoirs. Subsequently, the loaded therapeutic agents can be released slowly and continuously. For MNPs, due to their firm immobilization and extended retention in the gel matrix, a single injection can provide the capacity of multiple MHT.

Recently, a thermosensitive and NO-releasing hydrogel system made of polyester-PEG-polyester triblock copolymers end-capped by NO donors has been developed [57]. Nevertheless, the limited modification sites at the end of carrier copolymer significantly affected the loading amount of NO. Unlike polyester-based systems, many poly(amino acid) or polypeptide polymers have plentiful reaction sites on their side chains [40,51,58]. Obviously, polypeptide-based systems are more ideal candidates for achieving adequate modification of NO donors. So far, except for the hydrogel based on PEG-poly(L-arginine) copolymers [59], thermosensitive and NO-releasing hydrogels composed of PEG-polypeptide copolymers are still rare. Meanwhile, although some studies have employed injectable hydrogels as carriers of MHT [10,54,55,60–62], NO-synergized MHT and the enhancement of mild MHT through autophagy inhibition have not been reported.

Herein, a strategy based on autophagy inhibition mediated *via* a temperature-responsive hydrogel with sustained NO-releasing ability to amplify the efficacy of mild MHT was put forward. Firstly, to boost the loading amount of NO, a novel thermosensitive PEG-polypeptide copolymer decorated with abundant NO donors, α-(nitrate ester) acetic acid (NEAA), on its side chains (named as NO-polymer) was designed and synthesized. Simultaneously, according to the protocol previously

reported [10,63,64], we synthesized ferrimagnetic $Zn_{0.5}Fe_{2.5}O_4$ MNPs, which generate heat *via* the hysteresis loss mechanism. Subsequently, the mesoscopic self-assembly and macroscopic thermogelation behaviors of NO-polymers in water were examined. The effect of MNPs introduction on the thermo-induced sol-gel transition of NO-Gel composed of NO-polymers was investigated. The dispersity and heating performance of MNPs in NO-Gel were analyzed. The *in vitro* release profile of NO from MNPs@NO-Gel and the influence of heating on NO release were detected. The *in vivo* degradation of MNPs@NO-Gel and metabolism of released MNPs were studied. The *in vitro* and *in vivo* antitumor effects of MNPs@NO-Gel combined with or without multiple mild MHT were evaluated. Finally, the mechanism of NO-mediated enhancement of mild MHT was discussed and proposed. The schematic illustration of this study is presented in Fig. 1.

## 2. Results

### 2.1. Synthesis and characterization of PEG-polypeptide copolymers

Amino-terminated PEG ($NH_2$-PEG-$NH_2$) was synthesized *via* a 2-step reaction (Fig. S1a). The first step was to attain the intermediate product OMs-PEG-OMs *via* alcoholysis of the hydroxyl groups of PEG with methylsulfonyl chloride (MsCl). Next, in the presence of ammonia, the methylsulfonyl groups of OMs-PEG-OMs were replaced by amino groups to obtain $NH_2$-PEG-$NH_2$.

Subsequently, thermosensitive PEG-polypeptide copolymers modified with NO donors were synthesized through a 3-step process, as illustrated in Fig. 2a. Firstly, poly(L-alanine-*co*-β-benzyl-L-aspartate)-*b*-poly(ethylene glycol)-*b*-poly(L-alanine-*co*-β-benzyl-L-aspartate) (P(Ala-*co*-BLA)-PEG-P(Ala-*co*-BLA)) triblock copolymers were prepared *via* ring-opening copolymerization of L-Alanine *N*-carboxy-anhydride (L-Ala-NCA) and L-Aspartic acid 4-benzyl ester *N*-carboxy-anhydride (L-Asp (obzl)-NCA) using $NH_2$-PEG-$NH_2$ as the macroinitiator. Meanwhile, 18-crown-6 (18-C-6) was employed as the catalyst, which could both speed up polymerization and decrease side effects, as reported by Cheng et al. [65]. To endow the copolymer with the modifiable ability, the benzyl ether groups of P(Ala-*co*-BLA)-PEG-P(Ala-*co*-BLA) were replaced by ethanolamine (ETA), yielding P(Ala-*co*-Asp(ETA))-PEG-P(Ala-*co*-Asp (ETA)), which was rich in hydroxyl side chains. Finally, the NO donor NEAA was acquired (Fig. S2) and then modified onto the side chains of P (Ala-*co*-Asp(ETA))-PEG-P(Ala-*co*-Asp(ETA)) by esterification to obtain P (Ala-*co*-Asp(NO))-PEG-P(Ala-*co*-Asp(NO)) (NO-polymer). In addition, thermosensitive methoxy poly(ethylene glycol)-*b*-poly(L-alanine) (mPEG-PAla, called BK-polymer) was also synthesized by the same method (Fig. S3a and Fig. S4a).

The products obtained at each step were determined by $^1$H NMR analysis. As shown in Fig. S1b, the appearance of methyl peak at 3.10 ppm demonstrated that the methylsulfonyl group was successfully introduced to both ends of PEG. As the methylsulfonyl groups were replaced by amino groups, the methyl peak assigned to the methylsulfonyl group disappeared, while the peak of methylene adjoining to the amino group appeared at 2.91 ppm (Fig. S1b), indicating the successful synthesis of $NH_2$-PEG-$NH_2$. Meanwhile, $^1$H NMR analysis revealed that the amino substitution rate in $NH_2$-PEG-$NH_2$ was almost 100 %. The substitution degree in amino capped methoxy PEG (mPEG-$NH_2$) synthesized *via* the same method was also close to 100 % (Fig. S3B). Fig. 2b shows the $^1$H NMR spectra of PEG-polypeptide copolymers before and after the modification. Compared to P(Ala-*co*-BLA)-PEG-P(Ala-*co*-BLA), the benzene peak at 7.63 ppm was vanished and the ethylene peak of ETA appeared at 3.33 ppm, suggesting that P(Ala-*co*-Asp(ETA))-PEG-P(Ala-*co*-Asp(ETA)) was successfully obtained, and the substitution rate of ETA reached 95.0 %. Finally, the increased peak area at 4.86–5.08 ppm indicated that NEAA was conjugated to the side chains of P(Ala-*co*-Asp(ETA))-PEG-P(Ala-*co*-Asp(ETA)) copolymers, thus harvesting the desired NO-polymers. UV–Vis spectroscopic measurement further confirmed that the modification rate of NEAA in NO-polymers
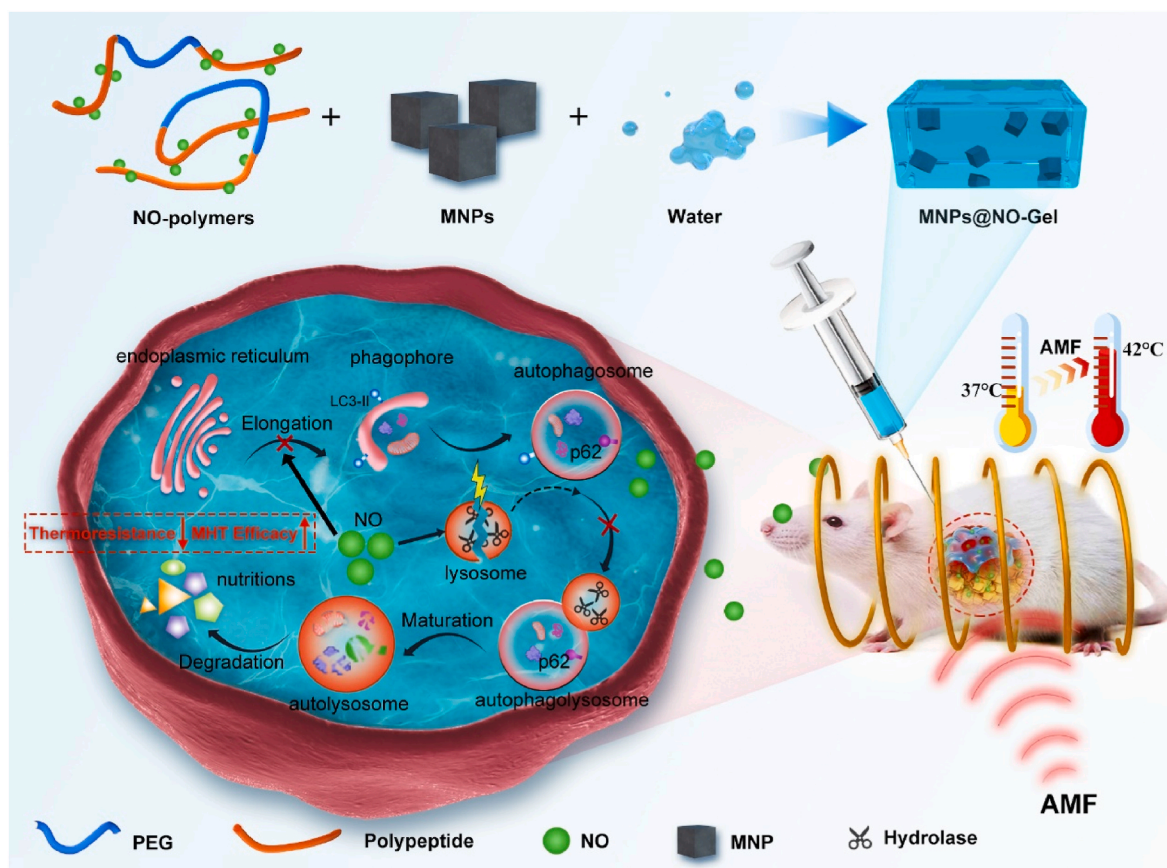
**Fig. 1.** Schematic illustration of the fabrication of MNPs@NO-Gel and the mechanism of released NO from MNPs@NO-Gel to enhance the efficacy of mild MHT through inhibiting autophagy. The MNPs@NO-Gel system composed of NO-polymers and MNPs was an injectable sol at low temperatures and exhibited a sol-gel transition upon heating. After injection at the tumor region, the MNPs@NO-Gel system *in situ* formed a hydrogel depot containing MNPs. Due to the homogeneous dispersion and strong immobilization of MNPs in NO-Gel, the MNPs@NO-Gel system possessed the ability of multiple mild MHT after only one administration. Meanwhile, mild MHT could accelerate the release of NO from the hydrogel matrix, and the released NO was diffused into tumor cells to inhibit the formation of autophagosomes and rupture lysosomes. As a result, the self-repairing autophagy pathway of tumor cells was blocked, resulting in a dramatic improvement in the efficacy of mild MHT.

reached as high as 89.4 % (Fig. S5). In addition, GPC analysis showed that both NO-polymer and BK-polymer presented a unimodal pattern (Fig. 2c and Fig. S4c). The molecular parameters of NO-polymer and BK-polymer characterized *via* $^1$H NMR and GPC are summarized in Table S1.

### 2.2. Synthesis and characterization of MNPs

$Zn_{0.5}Fe_{2.5}O_4$ MNPs were prepared through high-temperature decomposition of organic-metal ligands in a high-boiling point organic solvent according to previous studies [10,63,64]. The size and morphology of MNPs were confirmed by transmission electron microscopy (TEM). As shown in Fig. 2d, $Zn_{0.5}Fe_{2.5}O_4$ MNPs were uniform cubes with the size of approximately 70 nm. The element compositions of MNPs were analyzed *via* an inductively coupled plasma optical emission spectrometer (ICP-OES) system and a scanning electron microscope (SEM) equipped with an energy dispersive spectrometer (EDS). The result of ICP-OES analysis manifested that the weight ratio of Zn to Fe was 1:4.3, close to the stoichiometric composition of $Zn_{0.5}Fe_{2.5}O_4$ MNPs. EDS scanning revealed that the elements Zn, Fe, O were distributed evenly in MNPs (Fig. 2e). X-ray diffraction (XRD) pattern of MNPs was in line with that of standard $Fe_3O_4$ (PDF#19-0629) (Fig. 2f), indicating that MNPs maintained a spinel crystalline structure.

Moreover, the magnetic property of MNPs was also evaluated. As displayed in Fig. 2g, the magnetic hysteresis (*M-H*) curve of MNPs formed a hysteresis loop, and the coercivity ($H_c$) of $Zn_{0.5}Fe_{2.5}O_4$ MNPs was 31.5 Oe, while the saturated magnetization ($M_s$) was 113 emu/

$g_{(Zn+Fe)}$. This result demonstrates that $Zn_{0.5}Fe_{2.5}O_4$ MNPs are ferromagnets and can generate heat through the hysteresis loss mechanism under AMF [6].

### 2.3. Mesoscopic self-assembly and macroscopic phase transition behaviors of NO-polymers in water

Both NO-polymers and BK-polymers are amphiphilic and thus easy to self-assemble into micelles in water. Firstly, critical micelle concentrations (CMCs) of the two copolymers were determined by the circular dichroism (CD) spectroscopy. As shown in Figs. S6a and c, the CD spectra of polymer solutions exhibited a negative band with a minimum at 218 nm at low concentrations. As the concentration increased, the band red-shifted to 220–236 nm, indicating the formation of higher order structures such as micelles [50,66]. The fitting curves confirmed that the CMCs of NO-polymer and BK-polymer were 0.046 wt% and 0.060 wt%, respectively (Figs. S6b and d). Next, the size and morphology of micelles were observed *via* dynamic light scattering (DLS) and TEM. DLS results showed that the size of NO-micelles self-assembled by NO-polymers was *ca.* 30 nm at 15 °C or below and then increased with the elevation of temperature (Fig. 3a), implying that NO-micelles could aggregate under thermal actuation. TEM observation revealed that NO-micelles were dispersed at 10 °C (Fig. 3b) and formed clusters at 37 °C (Fig. 3c), which was consistent with the results determined by DLS. BK-micelles formed by BK-polymers exhibited a same variation trend with the elevation of temperature, as illustrated in
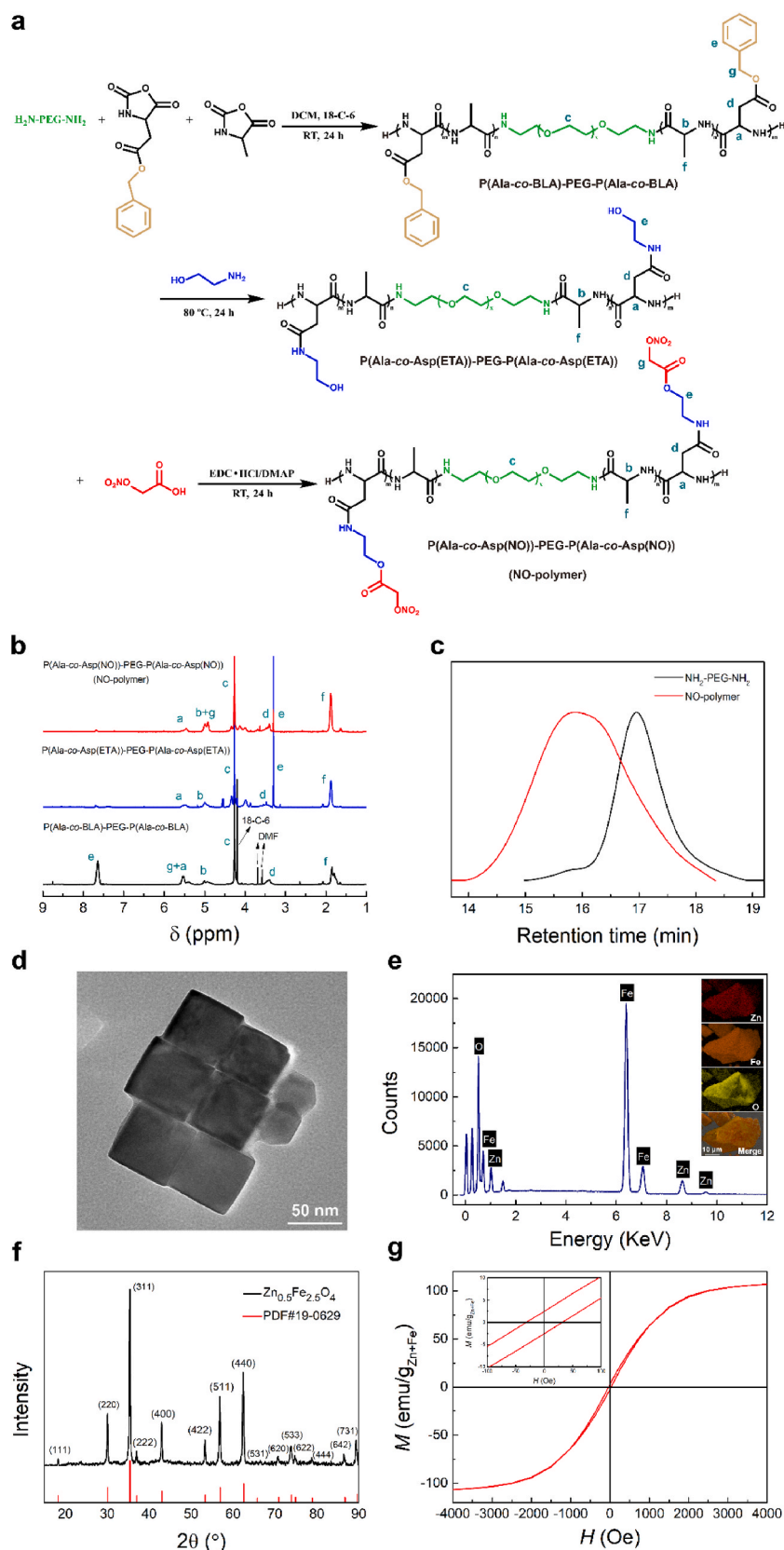
**Fig. 2.** Synthesis and characterization of NO-polymer and $Zn_{0.5}Fe_{2.5}O_4$ MNPs. (a) The synthesis route of NO-polymer. (b) $^1$H NMR spectra of P(Ala-*co*-BLA)-PEG-P(Ala-*co*-BLA), P(Ala-*co*-Asp(ETA))-PEG-P(Ala-*co*-Asp(ETA)) and NO-polymer. (c) GPC traces of $NH_2$-PEG-$NH_2$ and NO-polymer. (d) TEM observation of MNPs. (e) EDS analysis of MNPs. (f) XRD patterns of MNPs and standard $Fe_3O_4$. (g) *M-H* curve of MNPs measured at 300 K.
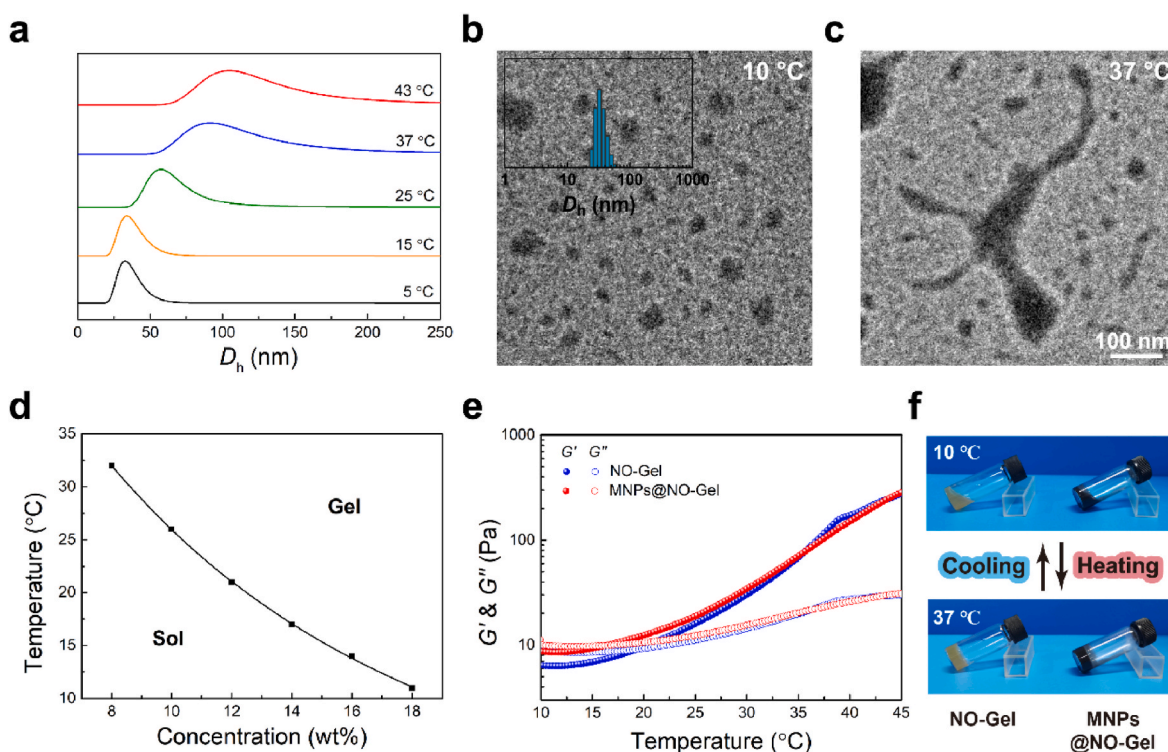
**Fig. 3.** Self-assembly and thermogelation behaviors of NO-polymers in water. (a) Size and distribution of NO-micelles (0.1 wt%) measured by DLS with the elevation of temperature. Morphology of NO-micelles (0.1 wt%) observed *via* TEM at (b) 10 °C and (c) 37 °C. (d) Phase diagram of NO-polymer/water system. (e) Rheological curves of NO-gel and MNPs@NO-gel as a function of temperature. (f) Optical images of NO-Gel and MNPs@NO-Gel at 10 °C and 37 °C. NO-Gel contained 13.5 wt% NO-polymers and MNPs@NO-Gel was loaded with 4 mg/mL of MNPs.

Figs. S7a–c.

When the concentration of NO-polymer was below 8 wt%, their aqueous solutions (named as NO-Gel solutions) always exhibited a sol state and no sol-gel transition was observed upon heating. In contrast, once the polymer concentration reached 8 wt% or higher, NO-Gel solutions were free-flowing sols at low temperatures but exhibited sol-gel transitions in response to increase of temperature. Fig. 3d and S7d display the phase diagrams of NO-polymer/water system and BK-polymer/water system, respectively, and their sol-gel transition temperatures ($T_{gel}$s) were significantly dependent on the polymer concentration. For example, as the concentration of NO-polymer increased from 8 wt% to 18 wt%, the $T_{gel}$ of NO-Gel decreased sharply from 32 to 11 °C. Considering the loading amount of NO and $T_{gel}$, we chose NO-Gel composed of 13.5 wt% NO-polymers for subsequent experiments.

Next, the thermo-induced gelation process of 13.5 wt% NO-Gel system was further studied *via* dynamical rheological analysis (Fig. 3e). The elastic modulus ($G'$) of NO-Gel system was lower than its viscous modulus ($G''$) at low temperatures, implying that the system was a low-viscous liquid. However, the $G'$ and $G''$ elevated spontaneously with the increase of temperature and the increasing rate of $G'$ was higher than that of $G''$. In general, the temperature at which $G'$ exceeds $G''$ is defined as $T_{gel}$ in rheological analysis [57,67]. The $T_{gel}$ of NO-Gel determined by rheological measurement was 19.5 °C, which was basically consistent with the result obtained from the phase diagram. The introduction of MNPs didn't affect the sol-gel transition of NO-Gel system, but reduced its $T_{gel}$ to 16.5 °C, and changed the system from yellow to black (Fig. 3e and f). To ensure the $T_{gel}$ of BK-Gel composed of BK-polymer was close to that of NO-Gel, the concentration of BK-polymer in BK-Gel was fixed at 8 wt%. Similarly, the incorporation of MNPs decreased the $T_{gel}$ of BK-Gel from 22.7 to 21.1 °C (Fig. S7e).

To further comprehend the mechanism of sol-gel transition of NO-Gel, the conformational variations of NO-polymers as a function of temperature were investigated using CD. CD spectra showed that the secondary structure of the polypeptide (P(Ala-*co*-Asp(NO)) block) was maintained in the temperature range of 10–40 °C (Fig. S8). The same phenomenon was also discovered in other thermosensitive polypeptide-based hydrogels [66,68]. On the other hand, PEG segments tend to dehydrate with the increase of temperature [38,66,68,69]. Therefore, we speculate that the amphiphilic NO-polymers first assemble into NO-micelles with hydrophilic PEG shells and hydrophobic polypeptide cores. As the temperature increases, a macroscopic physical hydrogel made up of a percolated micelle network is formed *via* the aggregation of NO-micelles and dehydration of PEG while maintaining the secondary structure of P(Ala-*co*-Asp(NO)) in this transition process, which is similar to other temperature-responsive hydrogel systems comprised of PEG-polypeptide copolymers [66,68].

### 2.4. Magnetic-heat conversion effect of MNPs

The magnetic-heat conversion efficiency of $Zn_{0.5}Fe_{2.5}O_4$ MNPs was evaluated in different media. At a fixed magnetic field intensity (*H*: 46.6 kA/m) and frequency (*f*: 300 kHz), the margin of temperature rising ($\Delta T$) of chloroform and NO-Gel loaded with 0.35 mg/mL MNPs within 120 s were 20.9 °C and 15.9 °C, respectively (Fig. 4a). The heating rate of MNPs in NO-Gel was lower than that of chloroform. This is due to the fact that the specific heat capacity of water (4.20 kJ/(kg·°C)) is much higher than that of chloroform (1.19 kJ/(kg·°C)), not because the heating performance of MNPs in NO-Gel is inferior to that in chloroform. Actually, the specific loss power (SLP) values of MNPs in chloroform and NO-Gel were 1474 W/g and 1878 W/g, respectively. The SLP is normalized by *H* and *f* to obtain the intrinsic loss power (ILP), which is a more objective parameter reflecting magnetic-heat conversion efficacy [70]. Accordingly, the ILP values of MNPs in chloroform and NO-Gel were 2.26 and 2.88 nH m$^2$/kg, respectively. However, compared to NO-Gel, the heating efficacy of MNPs in water declined sharply under the same conditions, and their SLP and ILP values were merely 342 W/g
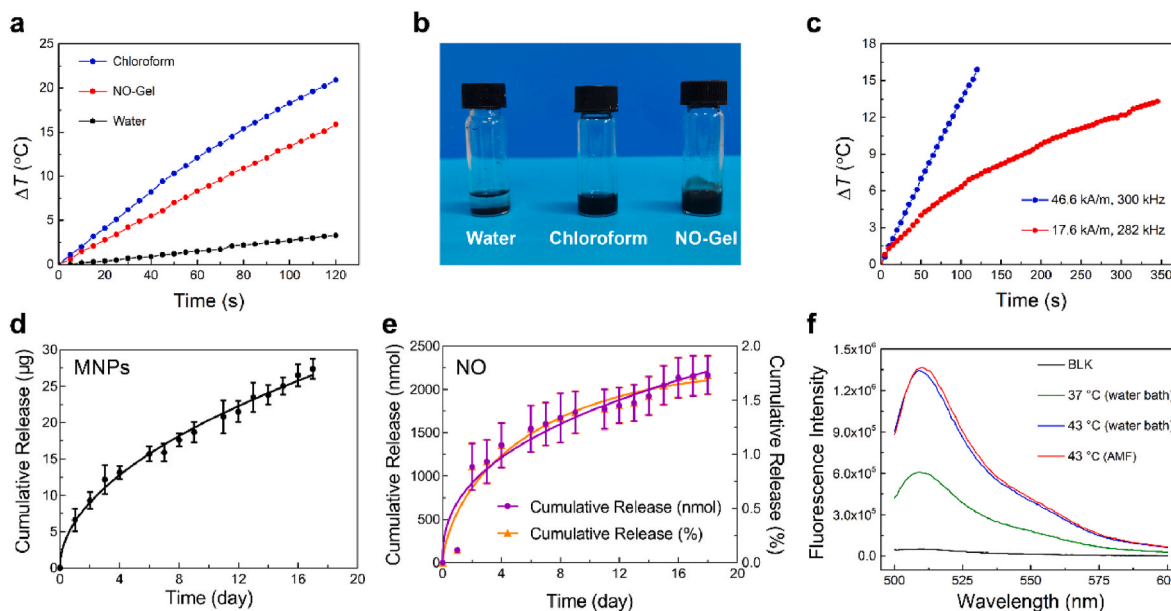
**Fig. 4.** Magnetic-heat conversion efficiency of MNPs and release behaviors of MNPs@NO-Gel *in vitro*. (a) Heating curves of MNPs in various media under AMF. The concentration of MNPs was 0.35 mg/mL; *H*: 46.6 kA/m; *f*: 300 kHz. (b) Optical images of MNPs in different media. (c) Heating curves of NO-Gel containing 0.35 mg/mL MNPs under different AMF conditions. *In vitro* release profiles of (d) MNPs and (e) NO from MNPs@NO-Gel (*n* = 3 for each group). The lines are just for guidance of eyes. Data are displayed as mean ± standard error of mean (SEM). (f) Fluorescence emission spectra of the release medium containing DAF-FM after MNPs@NO-Gel was treated for 30 min under different conditions.

and 0.52 nH m$^2$/kg, respectively. As displayed in Fig. 4b, MNPs were easy to aggregate and precipitate in water due to their magnetism. It is found that when the concentration of MNPs is very high, the magnetic interaction between MNPs is significantly higher than the anisotropy field, leading to a substantial decrease in the heating performance of MNPs [71,72]. Obviously, the aggregation/precipitation of MNPs in water is responsible for the severe weakening of its magnetic-heat conversion efficiency. In contrast, MNPs were uniformly dispersed in NO-Gel or chloroform. This phenomenon suggests that our NO-Gel has a merit to disperse MNPs evenly, which not only boosts the magnetic-heat conversion efficiency of MNPs but also achieves accurate heating.

Finally, considering that the magnetic field (*H* × *f*) lower than 5 × 10$^9$ A/(m·s) is safe for human MHT [6], we also explored the heating performance of MNPs under a lower magnetic field (*H*: 17.6 kA/m; *f*: 282 kHz). As shown in Fig. 4c, MNPs still exhibited good heating efficiency, and the SLP and ILP values of MNPs were 737 W/g and 8.44 nH m$^2$/kg, respectively.

### 2.5. In vitro release of MNPs and NO

The release curves of MNPs and NO *in vitro* from MNPs@NO-Gel were also investigated. The cumulative release amount of MNPs was 27 μg within 18 days (Fig. 4d), which was only 1.35 % of the theoretical loading amount. Given that thermosensitive hydrogel systems composed of PEG-polypeptide copolymers are usually very stable *in vitro* and can be degraded by proteases *in vivo* [38,68], the release profile of MNPs *in vivo* is more valuable, which was evaluated in the subsequent section. Meanwhile, the released NO was detected *via* the Griess kit assay. As presented in Fig. 4e, the release of NO exhibited a sustained manner and the total amount of released NO was 2170 nmol within 18 days, a more than two-fold increase over a previous hydrogel system comprised of PEG-polyester polymers end-capped by NO-donors [57]. However, it should be pointed out that the cumulative release rate of NO was only 1.73 %. The *in vitro* release of NO mainly depends on the decomposition rate of nitrate ester groups. Because of the slow decomposition rate of nitrate ester at 37 °C [57], the *in vitro* release amount of NO from NO-Gel was low. Such a slow release of NO *in vitro* has also been observed in

other systems modified with nitrate esters [23,57].

Furthermore, the influence of heating on NO release was explored. A NO fluorescence probe 4-aminomethyl-2′,7′-difluorescein (DAF-FM) was added into the release medium, and subsequently the MNPs@NO-Gel system containing the release medium was incubated in a 37 °C/43 °C water bath or heated to 43 °C with AMF. After 30 min of treatment, the fluorescence intensity of the release medium was detected. As displayed in Fig. 4f, water bath or AMF-induced heating obviously accelerated the release of NO.

### 2.6. In vitro cytocompatibility of NO-polymer and BK-polymer

Good biocompatibility is a basic requirement for medical materials/devices [73–77]. Therefore, *in vitro* cytocompatibility of the synthesized NO-polymer and BK-polymer to normal mouse embryo fibroblast NIH3T3 cells was evaluated *via* the cell counting kit-8 (CCK-8) assay [78]. As presented in Fig. S9, the cell viability of BK-polymer always exceeded 85 % in the measured concentration range. When the content of NO-polymer was 500 μg/mL, the viability of NIH3T3 cells was as high as about 95 %. As the NO-polymer concentration further increased to 1000 μg/mL, the cell viability decreased somewhat but remained above 75 %. The decline in the cytocompatibility of NO-polymer at high concentrations should be attributed to the increased release of NO in cells.

### 2.7. Cellular uptake of NO-micelles and intracellular release of NO

First of all, to visualize the uptake of NO-micelles by tumor cells, a hydrophobic fluorescence probe coumarin-6 (Co-6) was loaded into the cores of NO-micelles. As presented in Fig. S10, NO-micelles containing Co-6 were efficiently endocytosed by CT-26 tumor cells. Then, the intracellular release of NO from NO-micelles was confirmed by utilizing 4-aminomethyl-2′,7′-difluorescein diacetate (DAF-FM DA), which is converted into fluorescence probe DAF-FM in cells to detect intracellular NO (Fig. S11). The CT-26 cells showed only faint green fluorescence in the BK-micelles-treated group, as depicted in Fig. 5a. After incubation with NO-micelles, the cells showed markedly enhanced green fluorescence. Particularly, the green fluorescence of the cells treated with NO-
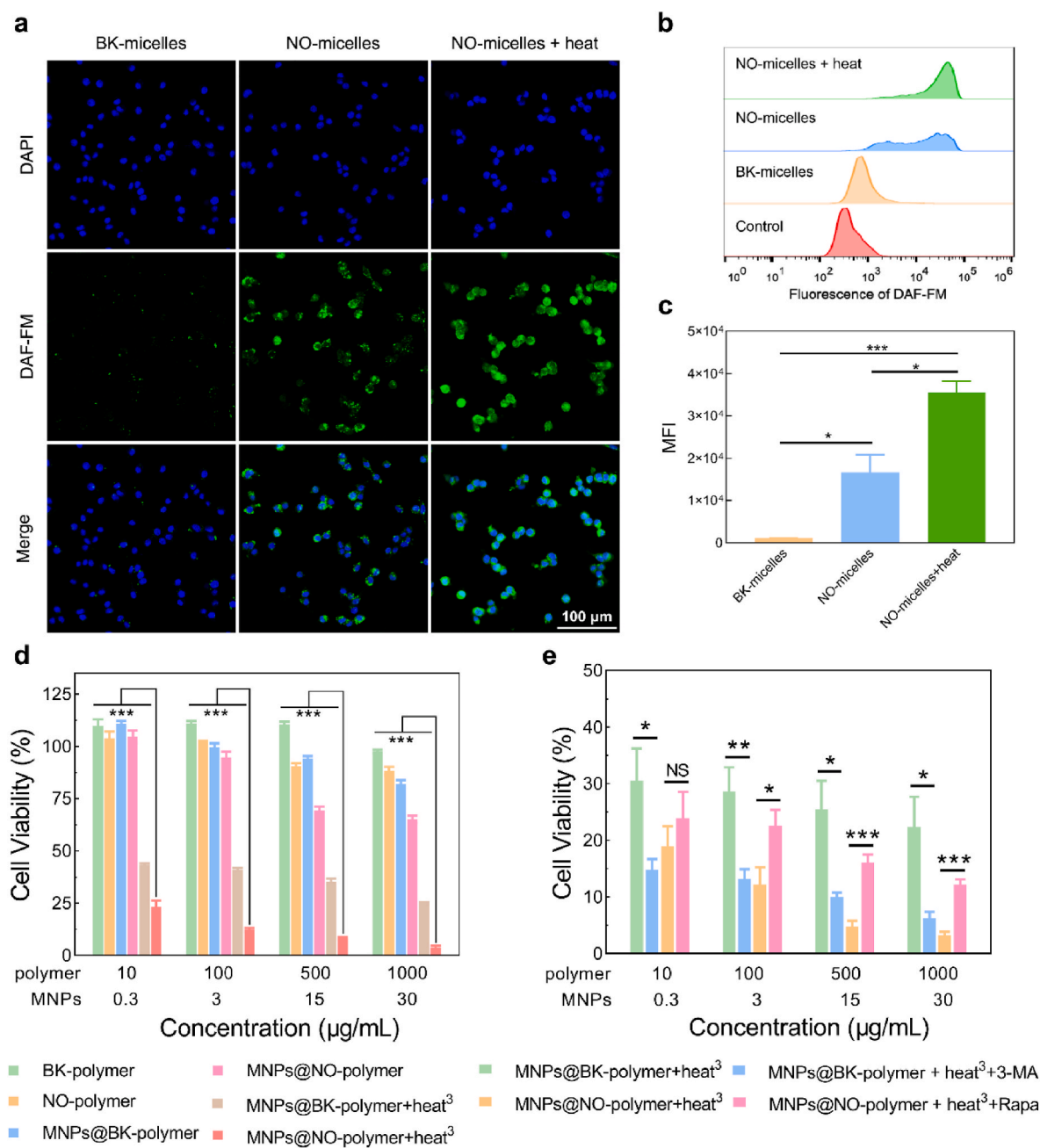
**Fig. 5.** (a) Fluorescence images of CT-26 cells stained with 4′,6-diamidino-2-phenylindole (DAPI, blue) and DAF-FM (green) to detect intracellular NO after various treatments. Heat meant that the cells were treated at $42.5 \pm 0.5\ °C$ for 20 min. (b) Flow cytometry analysis of DAF-FM intensity to detect intracellular NO and (c) the corresponding mean fluorescence intensity (MFI). The control group indicated that CT-26 cells were treated with culture medium only and not stained with DAF-FM. For each group, $n = 3$. (d) Viability of CT-26 cells after various treatments. For each group, $n = 6$. (e) Viability of CT-26 cells treated with MNPs@BK-Polymer + heat[3] with/without 3-MA or treated with MNPs@NO-polymer + heat[3] with/without Rapa. Heat meant that the cells were treated at $42.5 \pm 0.5\ °C$ for 20 min and the superscript "3" indicates the treatment number. Data are displayed as mean $\pm$ SEM. For each group, $n = 6$. *$p < 0.05$, **$p < 0.01$, ***$p < 0.001$; NS: not significant.

micelles became brighter after 20 min culture in a $42.5 \pm 0.5\ °C$ water bath (the group of NO-micelles + heat). This feature was further confirmed through flow cytometry (Fig. 5b and c), suggesting that the internalized NO-micelles can release NO in CT-26 cells and heating facilitates this process. Different from the release mechanism of NO *in vitro*, the intracellular release of NO is attributed to the abundant glutathione in tumor cells, which can reduce the nitrate ester groups to generate NO [23,57,79].

## 2.8. In vitro anticancer effect

The *in vitro* anticancer activity of MNPs-loaded copolymers combined with or without mild thermal therapy against CT-26 cells was assessed. In the MNPs loading groups, the weight ratio of copolymers to MNPs was set to 100:3. As displayed in Fig. 5d, BK-polymer and NO-polymer themselves had no significant inhibitory effect on CT-26 cells even at the concentration of 1000 μg/mL. The introduction of MNPs increased the anticancer activities of MNPs@BK-polymer and MNPs@NO-polymer. When the copolymer concentration was 1000 μg/mL and the MNPs content was 30 μg/mL, the cell viability of MNPs@BK-

polymer system reduced to 82.1 % and that of MNPs@NO-polymer system was only 65.1 %. The reason for the enhanced anticancer efficacy of MNPs@BK-polymer might be that $Fe^{2+}$ degraded from MNPs could react with intracellular $H_2O_2$ to generate active ·OH through Fenton reaction. Because ·OH can degrade methylene blue (MB), we utilized MB to determine the occurrence of Fenton reaction. As shown in Fig. S12, only in the presence of $H_2O_2$ and MNPs that were pre-treated with HCl solution, MB was gradually degraded, implying that $Fe^{2+}$ released from MNPs could trigger Fenton reaction to produce ·OH. As to MNPs@NO-polymer, the generated ·OH could cascade with NO liberated from NO-polymers and intracellular $H_2O_2$ to produce more lethal peroxynitrite anion ($ONOO^-$). This was also confirmed via an *in vitro* experiment. As presented in Fig. S13, after mixing NO-micelles, $H_2O_2$ and MNPs pre-treated with HCl solution with $ONOO^-$ probe and incubating them at 37 °C for 3 h, a strong fluorescence peak assigned to $ONOO^-$ appeared, indicating that $ONOO^-$ was indeed generated via the cascade reaction of ·OH, $H_2O_2$ and released NO. A similar phenomenon has been observed in previous studies [37,57].

After treatment with MNPs@BK-polymer combined with triple mild thermal therapy, the viability of CT-26 cells decreased sharply to 24.9 % at the same concentration (the polymer concentration: 1000 μg/mL; the MNPs concentration: 30 μg/mL). Amazingly, almost all cells in the MNPs@NO-polymer + heat[3] group were killed at this concentration, leaving only 3.8 % cell viability. This finding suggests that the NO released from NO-polymers can significantly boost the anticancer efficacy of mild thermal therapy and the MNPs@NO-polymer system plus three mild hyperthermia is sufficient to achieve a satisfactory antitumor effect.

### 2.9. NO-induced autophagy inhibition

It has been reported that NO could suppress the subcellular degradation process, such as autophagy, thus accelerating cellular apoptosis [13,30]. To verify whether the enhanced effect of NO-polymer on thermal therapy was related to the inhibition of autophagy, the autophagy inhibitor 3-methyladenine (3-MA) was introduced into the MNPs@BK-polymer system during thermal treatment, while the autophagy inducer rapamycin (Rapa) was incorporated into MNPs@NO-polymer. As presented in Fig. 5e, compared to the MNPs@BK-polymer + heat[3] group, the addition of 3-MA dramatically improved the therapeutic efficacy of MNPs@BK-polymer + heat[3] + 3-MA system. In contrast, due to the introduction of Rapa, the inhibitory effect of MNPs@NO-polymer + heat[3] + Rapa system was greatly offset when compared with the MNPs@NO-polymer + heat[3] group. These results provide strong evidence to support that the inhibition of autophagy induced by NO-polymer is responsible for the enhanced efficacy of thermal therapy.

Encouraged by the above findings, we further explored the mechanism of autophagy-based protection triggered by mild thermal therapy and revealed the role of NO in this process. Microtubule-associated protein 1 light chain 3B (LC3B) is a classical protein related to autophagy. When autophagy is activated, LC3B–I, the cytosolic form of LC3B, is converted into lipidated LC3B-II, a membrane-bound protein, and recruited to the membrane of autophagosome [80]. Hence, the expression level of LC3B-II protein in CT-26 tumor cells receiving diverse interventions were assayed by Western blot. As shown in Fig. 6a, c, and d, after the cells were treated with the MNPs@BK-micelles + heat system, the ratios of LC3B-II/LC3B–I and LC3B-II/β-actin were significantly upregulated, implying that mild hyperthermia indeed induced autophagy. In contrast, after CT-26 cells were treated with the MNPs@NO-micelles + heat system, LC3B-II level was downregulated evidently in comparison with the former system, demonstrating that the NO released from NO-micelles suppressed mild hyperthermia-induced autophagy.

Moreover, sequestosome 1 (SQSTM1, also called p62), a ubiquitin-binding protein, is a selective substrate of autophagy, which is recruited to autophagosomal membrane and specifically degraded in autolysosomes after autophagosomes fuse with lysosomes [30,80,81]. Therefore, p62 expression was also evaluated *via* an automated capillary Western blot system, and this methodology has been adopted in many studies [82–84]. The chemiluminescence intensity of various samples was measured (Fig. S14) and the areas under curves were calculated and transformed into Western blot strips, as shown in Fig. 6b. The quantitative ratio of p62/β-actin is presented in Fig. 6e. Compared to the MNPs@BK-micelles group, p62 expression in the MNPs@BK-micelles + heat group was markedly downregulated, indicating that the lysosomes were activated by thermal treatment and formed autolysosomes with the autophagosomes. However, p62 levels in all the NO-micelles treatment-related groups were elevated evidently, even in the MNPs@NO-micelles + heat group. A similar result was also found in a relevant work [13]. According to a previous study [85], NO could alter the redox balance of lysosomes, and thus we speculate that NO may damage the lysosomes, thereby interfering with the fusion of lysosomes and autophagosomes. As a consequence, the degradation of p62 is blocked, resulting in the accumulation of p62 in autophagosomes in the NO-micelles treatment-related groups.

To further validate the impact of NO on autophagosomes and lysosomes, CT-26 cells were co-stained with CYTO-ID and Lysotracker red, and then observed with a confocal laser scanning microscope (CLSM). CYTO-ID is a dye specific for autophagosomes with green fluorescence emission [13,29], while Lysotracker red is a fluorescence probe that can specially mark lysosomes [30,81]. We found that MNPs could disturb the signal of CYTO-ID and thus MNPs were excluded in this experiment. As depicted in Fig. 6f, compared to the BLK and BK-micelles groups, both green and red fluorescence were enhanced in cells after being treated with BK-micelles + heat, indicating that mild hyperthermia-induced autophagy led to the proliferation of autophagosomes and the activation of lysosomes. More interestingly, many green puncta of autophagosomes overlapped with many red puncta of lysosomes, forming yellow spots in their merge image, implying that the autophagosomes fused with the lysosomes, resulting in the formation of autolysosomes. However, in the NO-micelles and NO-micelles + heat groups, both green and red fluorescence were remarkably diminished, especially red fluorescence representing lysosomes, substantiating that the sufficient supply of NO in cells not only significantly depressed the formation of autophagosomes but also had a potent destructive effect on lysosomes. The quantitative fluorescence ratio of Lysotracker red to DAPI (Fig. 6g) and statistical data of CYTO-ID fluorescence intensity obtained from flow cytometry (Fig. 6h and i) further supported the above favorable outcome.

### 2.10. Degradation of NO-gel and metabolism of MNPs in vivo

To invasively monitor the degradation of NO-Gel *in vivo*, a rhodamine (RB)-labeled macromolecular fluorescence probe (RB-PAla-PEG-PAla-RB) was prepared (Fig. S15a) as previously described [49]. Subsequently, RB-PAla-PEG-PAla-RB-encapsulated NO-Gel was hypodermically administered into the back of BALB/c mice and its degradation *in vivo* was visualized by fluorescence imaging. As illustrated in Figs. S15b–c, the total fluorescence intensity of NO-Gel continuously receded with the passage of time, indicating its gradual degradation. Meanwhile, based on the change of fluorescent intensity, we further validated that the *in vivo* persistence of NO-Gel was over 35 days.

The degradation of MNPs@NO-Gel system and the metabolism of MNPs *in vivo* were also investigated. After hypodermic injection of MNPs@NO-Gel into BALB/c mice, three mice were randomly sacrificed at each sampling time to observe the remaining MNPs@NO-Gel. Representative optical images of mice containing remaining MNPs@NO-Gel are presented in Fig. 7a. The degradation of MNPs@NO-Gel seemed to be more steady and slower than that of NO-Gel itself (Fig. 7b). It is credited to the introduction of MNPs, which elevates the hydrophobicity of the NO-Gel system. Meanwhile, to evaluate the *in vivo*
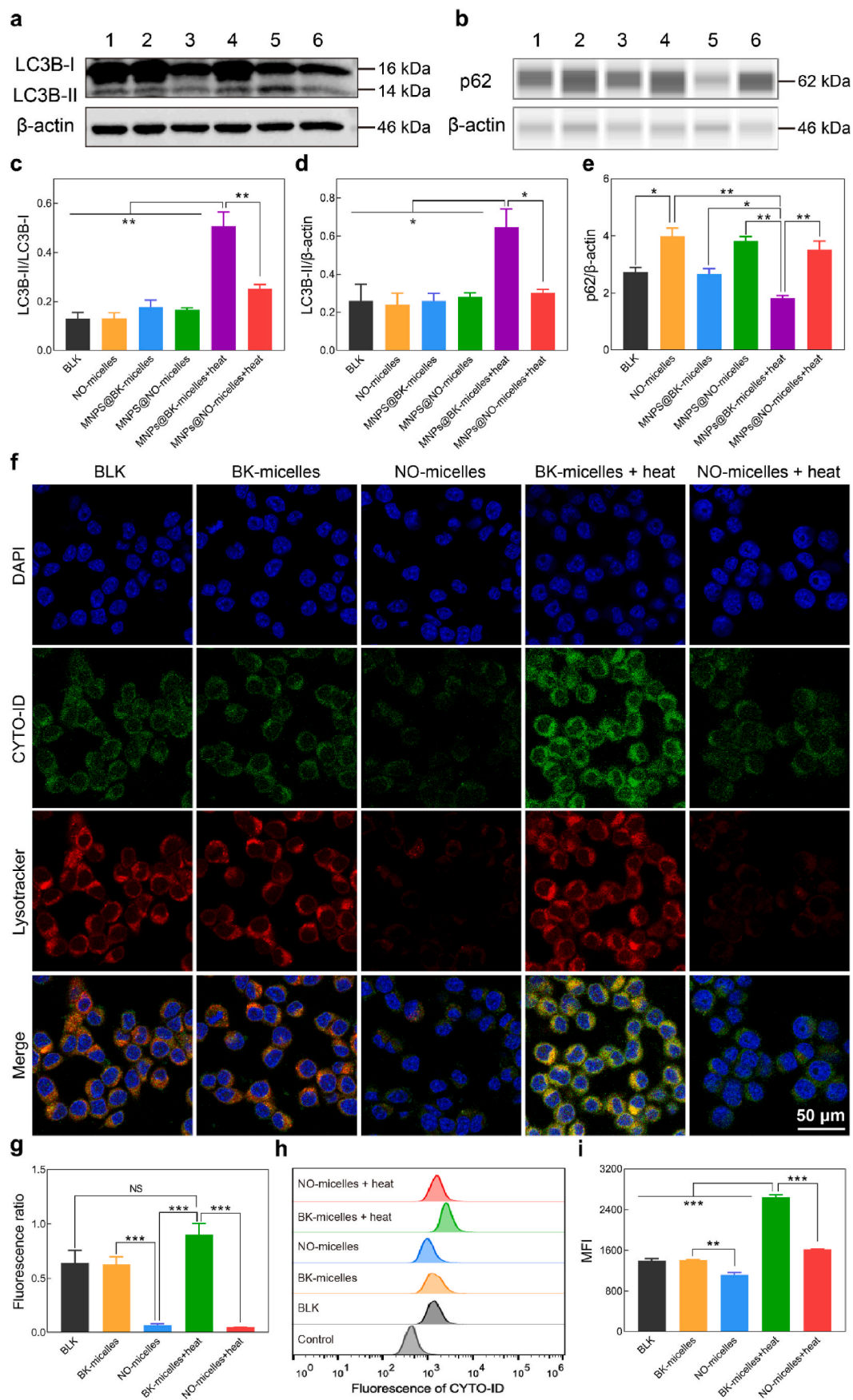
**Fig. 6.** Mechanism analysis of NO-induced autophagy inhibition. (a) Expression of LC3B assayed by a traditional Western blot system and (b) Expression of p62 assayed by an automated capillary Western blot system. **1**: the BLK group, in which the CT-26 cells only received the treatment of culture medium; **2**: the NO-micelles group; **3**: the MNPs@BK-micelles group; **4**: the MNPs@NO-micelles group; **5**: the MNPs@BK-micelles + heat group; **6**: the MNPs@NO-micelles + heat group. Heat meant that the cells were treated at 42.5 ± 0.5 °C for 20 min. The concentrations of copolymer and MNPs were 1000 μg/mL and 30 μg/mL, respectively. The quantitative ratios of LC3B-II/LC3B–I (c), LCB-II/β-actin (d) and p62/β-actin (e). For each group, $n = 3$. (f) Fluorescence images of CT-26 cells stained with CYTO-ID (green) and Lysotracker red (red) to detect autophagosomes and lysosomes, respectively. (g) Fluorescence ratio of Lysotracker red to DAPI in (f). For each group, $n = 4$. (h) Flow cytometry analysis of CYTO-ID intensity to detect autophagosomes and (i) the corresponding MFI. CT-26 cells that were treated with culture medium only and not stained with CYTO-ID was employed as the control group. For each group, $n = 3$. Data are displayed as mean ± SEM. *$p < 0.05$, **$p < 0.01$, ***$p < 0.001$; NS: not significant.
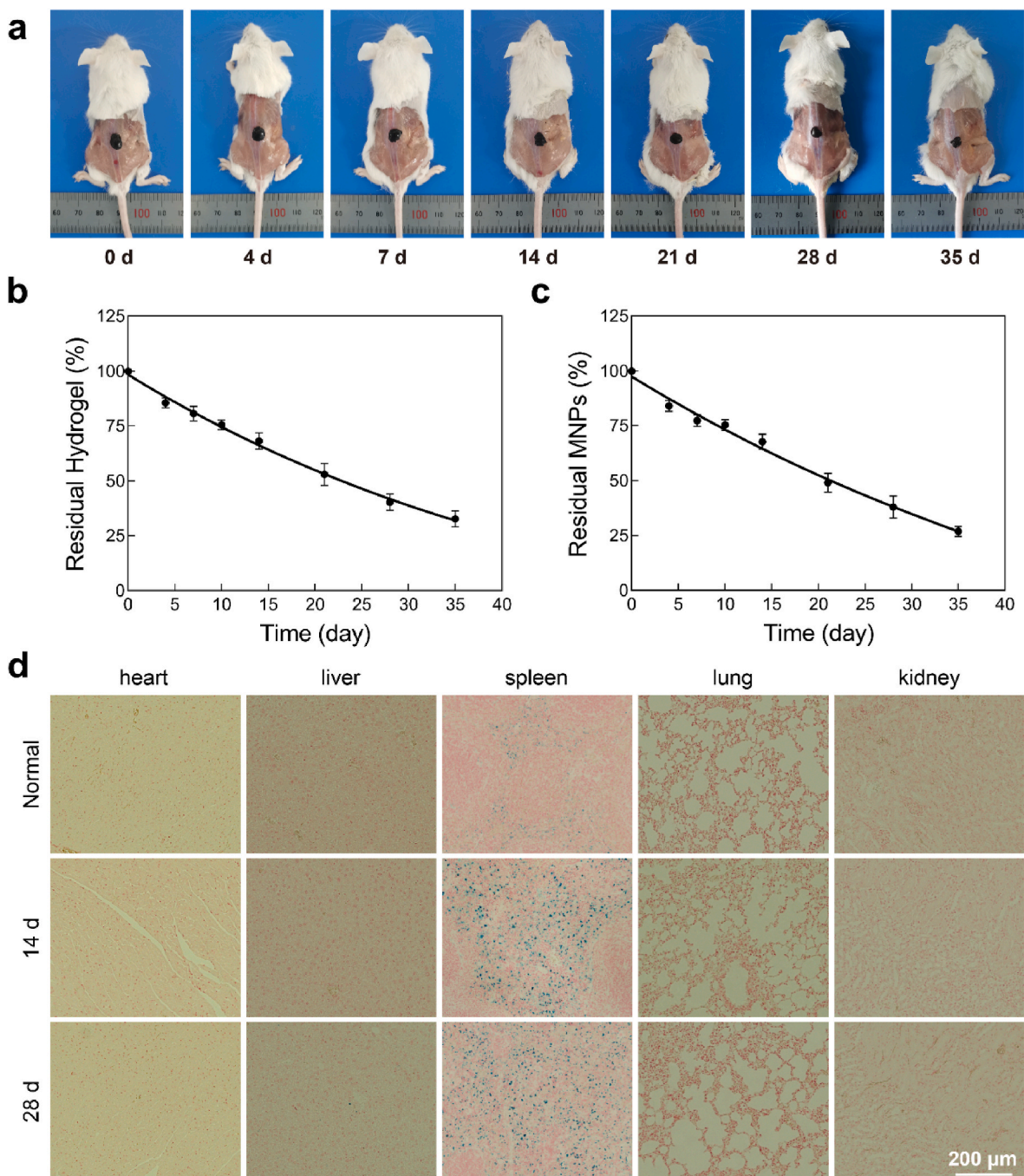


**Fig. 7.** Degradation of MNPs@NO-Gel and release/metabolism of MNPs *in vivo*. (a) Representative optical images of mice treated with MNPs@NO-Gel and dissected at predetermined time points. (b) Degradation curve of MNPs@NO-Gel *in vivo* ($n = 3$). (c) Release profile of MNPs *in vivo* ($n = 3$). Data are displayed as mean ± SEM. (d) Prussian blue-stained slices of main organs.

release of MNPs, the content of MNPs in the remaining MNPs@NO-Gel was measured *via* ICP-OES. As displayed in Fig. 7c, the release curve of MNPs was in agreement with the degradation profile of MNPs@NO-Gel, suggesting that the degradation of NO-Gel *in vivo* controlled the *in vivo* release of MNPs. In particular, only 14.4 % of MNPs was released within the initial 4 days, which endowed the ability to conduct multiple MHT after only one injection of MNPs@NO-Gel.

Additionally, considering that iron(III) ions in cells can be specifically stained by Prussian blue [86], the main organs of mice were harvested, sliced and stained with Prussian blue. As presented in Fig. 7d, no tissue abnormalities were observed; nevertheless, compared to the spleens of normal mice, a lot of blue dots were observed in the spleens of mice treated with MNPs@NO-Gel on day 14 and 28 post-injection, suggesting the released MNPs were mainly metabolized through the spleen.

### 2.11. In vivo antitumor efficacy

BALB/c mice were inoculated with CT-26 tumor cells. When the tumors reached about 100 mm$^3$, the tumor-bearing mice were treated with different formulations. For the MNPs@NO-Gel + MHT$^3$ group, the mice received mild MHT three times on day 0, day 2, and day 4 after the injection of MNPs@NO-Gel. The AMF condition was set as $H = 17.6$ kA/m and $f = 282$ kHz, which is safe for mice and humans ($H \times f < 5 \times 10^9$ A/(m·s)) [6]. The average temperature of tumor zone was maintained at $42.5 \pm 1.0$ °C for 20 min at each MHT. The heating curves of tumor region during each MHT and the corresponding infrared thermal images of mice at different time points during each MHT are displayed in Fig. 8. The results showed that the tumor could be heated to the target temperature in about 6 min for all 3 MHT cycles. This is credited to the high magnetic-to-thermal conversion efficiency of MNPs plus the firm immobilization of MNPs in NO-Gel. Conversely, the tumor-bearing mouse treated with AMF alone and not injected with MNPs@NO-Gel did not experience temperature rising in the tumor area.

Fig. 9a depicts the treatment schedule, and the curves of tumor growth are drawn in Fig. 9b. Compared to the BLK group, treatment with NO-gel and MNPs@BK-Gel had no remarkably antitumor effects. The treatment of MNPs@NO-Gel partially restrained tumor growth thanks to the generation of lethal ONOO$^-$, which has been discussed in section 2.8. Tumor growth was prominently suppressed in the MNPs@BK-Gel + MHT$^3$ group, which was attributed to the MHT-induced thermal effect. Astonishingly, all the tumors were thoroughly eliminated in the MNPs@NO-Gel + MHT$^3$ group. It was because that NO liberated from NO-Gel effectively inhibited mild hyperthermia-induced cellular autophagy, resulting in that the effect of mild MHT in the MNPs@NO-Gel + MHT$^3$ group was dramatically strengthened. This was in accordance with the *in vitro* anticancer outcome (Fig. 5d).

In addition, it is worth noting that after receiving MHT three times, the skin of mice appeared obvious scabs, but the scabs healed basically within three weeks (Fig. S16), suggesting that the damage of mild MHT to the skin was reversible and repairable.

On day 14 of the treatment, one mouse was euthanized at random in each group, and then the tumors were dissected and photographed. Fig. 9h shows the optical images of collected tumors. The tumor size of each group was consistent with their tumor growth curves, and indeed, no residual tumor was found in the MNPs@NO-Gel + MHT$^3$ group. Next, the tumors were stained with hematoxylin and eosin (H&E) and terminal deoxynucleotidyl transferase-mediated dUTP-biotin nick end labeling (TUNEL). As presented in Fig. 9h, only the tumor in the MNPs@BK-Gel + MHT$^3$ group showed obvious necrosis and apoptosis regions, which was also in line with the results in Fig. 9b.

Subsequently, the survival period of the remaining mice in each group was evaluated. As shown in Fig. 9d, the survival rate of mice also depended on the antitumor effect of the therapy system. The better the antitumor effect of the formulation used, the longer the survival rate of the mice. In particular, all the mice treated with MNPs@NO-Gel + MHT$^3$
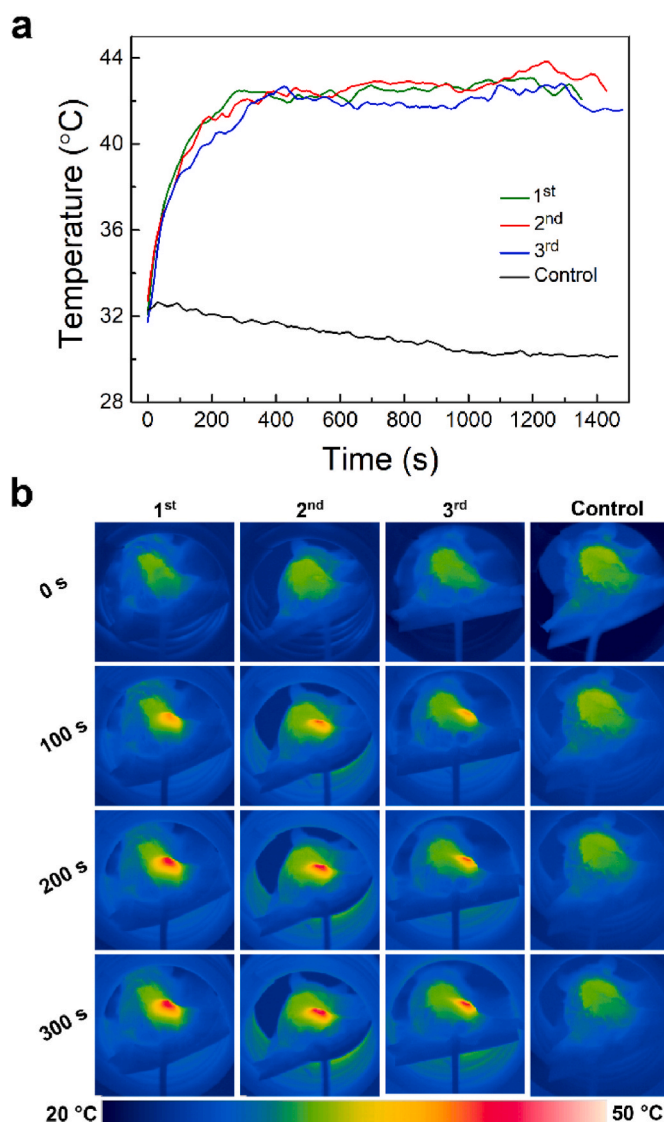
**Fig. 8.** Three MHT treatments of mice bearing CT-26 tumor after a single injection of MNPs@NO-Gel. (a) Heating curves of tumor region during 3 cycles of MHT. A tumor-bearing mouse that only received AMF treatment was select as the control group. (b) Infrared thermal images of mice at different time points during 3 cycles of MHT. The loading amount of MNPs was 4 mg/mL. The injection volume of hydrogel was 0.2 mL per mouse.

were alive throughout the whole survival experiment. Fifty days later, the mice in the MNPs@NO-Gel + MHT$^3$ group were humanely euthanized. As presented in Fig. S17, there was no residual tumor at the primary tumor site, which was further confirmed by autopsy observations. This strongly proved that the NO-enhanced multiple mild MHT did indeed completely eradicate the CT-26 tumors and there was still no tumor recurrence on day 50 post-treatment. Meanwhile, it should be pointed out that the remnant amount of MNPs@NO-Gel in different mice were diverse (Fig. S17b), and this was credited to their individual differences.

During the survival experiment, after the dead/euthanasia of each group of mice, their main organs (heart, liver, spleen, lung and kidney) were harvested, weighed and stained with H&E. Meanwhile, the whole blood and serum of euthanized mice were collected to detect the blood routine indexes and liver & renal functions. As presented in Fig. 9e, obvious splenomegalia was observed in all other groups except the MNPs@NO-Gel + MHT$^3$ group, whose spleen weight was analogous to that of healthy animals. This was attributed to the accumulation of
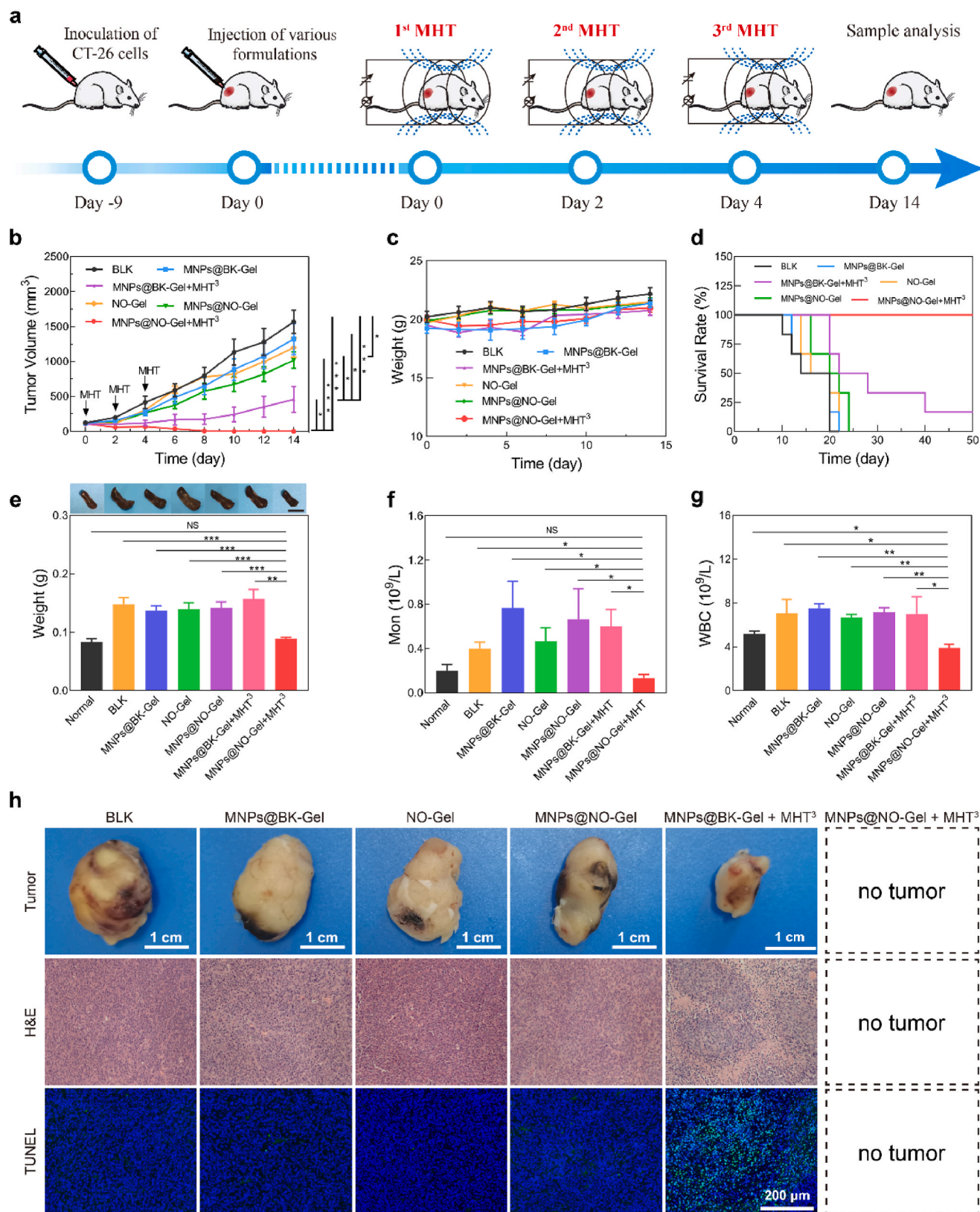
**Fig. 9.** Treatment efficacy *in vivo*. (a) Schematic illustration of treatment schedule. (b) Tumor growth curves of mice receiving various treatments ($n = 7$). (c) Body weight variations of mice after various treatments ($n = 7$). (d) Survival curves of mice after different treatments ($n = 6$). When tumor grew to 2000 mm³, the mouse was euthanized humanely according to animal ethics. (e) Spleen weight of mice in diverse groups ($n = 6$). The spleens were collected when the mice were euthanized. The upper optical images are the representative spleens of each group and the scale bar is 1 cm. (f) Mon and (g) WBC levels of mice in different groups ($n = 6$). The blood specimens were gathered when the animals were euthanized. (h) Optical, H&E and TUNEL staining images of tumors obtained on day 14. The tumor was totally eliminated in the MNPs@NO-Gel + MHT³ group. Data are displayed as mean ± SEM. *$p < 0.05$, **$p < 0.01$, ***$p < 0.001$; NS: not significant.

splenic granulocytes from the peripheral blood and/or the splenic granulopoiesis through the tumor-induced leukemoid reaction with rapid tumor progression [87]. In addition, the levels of monocytes (Mon) and white blood cells (WBC) in all the other 5 groups were greater than those of healthy animals except for the MNPs@NO-Gel + MHT[3] group (Fig. 9f and g), indicating that the continuous development of tumors caused systematic inflammatory response. These findings strongly suggest that only inhibiting tumor growth without eradicating the tumor completely does not prevent the development of these complications related to tumors.

The *in vivo* biocompatibility of different therapy systems combined with or without MHT was appraised. After various treatments, the body weight of mice in each group exhibited an increasing trend (Fig. 9c). Meanwhile, there were no histologic changes in the main organs of mice in each group on day 14 (Fig. S18). In addition, the blood routine indexes and liver and renal function indexes of euthanized mice in each group were similar to normal mice or within the normal range (Figs. S19–S20). These outcomes confirm that all the therapeutic systems have good biocompatibility and no evidently systematic side effects on mice. We also conducted another experiment to evaluate the acute toxicity of the MNPs@BK-Gel + MHT[3] and MNPs@NO-Gel + MHT[3] systems. After the CT-26 tumor-bearing mice received a single injection of MNPs@BK-Gel/MNPs@NO-Gel plus triple MHT, their whole blood and serum were collected on day 5. As shown in Figs. S21–S22, all the values of blood routine indexes and liver and renal functions were analogous to healthy animals or within the normal range as well, indicating that the administration of MNPs@BK-Gel/MNPs@NO-Gel plus following multiple MHT did not give rise to acute toxicity in mice.

Finally, the expression levels of LC3B-II and p62 in the tumor tissues were assayed by immunofluorescence staining after the tumor-bearing mice received MHT only once. As shown in Fig. 10a and S23, LCB-II expression was downregulated obviously, while p62 expression was elevated dramatically in the MNPs@NO-Gel + MHT group compared to the MNPs@BK-Gel + MHT group. This indicates that the sufficient supply of NO can prevent the formation of autophagosomes and directly destroy lysosomes to inhibit autophagy-mediated self-repairing. Fig. 10b illustrates the proposed mechanism of NO-mediated autophagy inhibition. As a consequence, the antitumor efficacy of mild MHT was remarkably boosted, resulting in the thorough elimination of CT-26 colon tumors, as demonstrated in Fig. 9b and h.

## 3. Discussion

Autophagy is a cellular self-protecting pathway activated by cellular stresses, especially thermal stress, which is one of main reasons for the thermal resistance of tumors induced *via* mild hyperthermia [13,14,16, 18]. Although NO can inhibit autophagy flux, only a few nano-delivery systems containing NO donors have been developed to improve the antitumor efficacy of mild photothermal therapy [13]. Meanwhile, the enhancement effect is still limited due to the insufficient supply of NO in tumors.

To address this issue, a novel thermosensitive hydrogel with long-acting NO-releasing performance was designed and prepared in this study. To increase the loading amount of NO, PEG-polypeptide triblock copolymers with plentiful modifiable side groups were first synthesized (Fig. 2a). Then, NO donor NEAA was conjugated to their side chains to attain NO-polymers (Fig. 2a). NO-polymers readily self-assembled into NO-micelles in an aqueous system (Fig. 3a and b), and its concentrated aqueous system (13.5 wt%) exhibited a sol-gel transition with increasing temperature and formed a non-flowing NO-Gel at body temperature (Fig. 3d–f). The mechanism of NO-Gel formation is attributed to the aggregation of NO-micelles and dehydration of PEG upon heating (Fig. 3a and c). On account of abundant modifiable sites on the side chains of NO-polymer plus the high modification efficiency of NO donor, the loading amount of NO in NO-Gel reached 228 μmol/mL, which was 2.5 times that of the hydrogel composed of NO donor capped polyester-PEG-polyester copolymers reported previously [57].

MHT has been widely concerned in clinic owing to the characteristics of excellent penetration depth and non-invasive administration in comparison with other hyperthermia strategies [4,6,9]. However, MHT
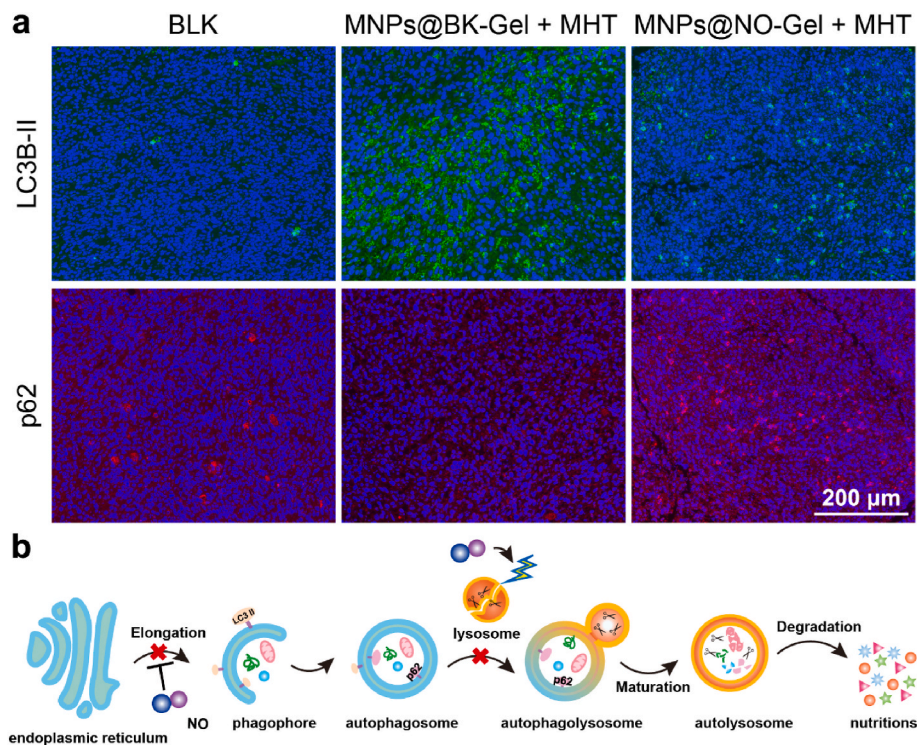


**Fig. 10.** (a) LC3B-II and p62 immunofluorescent staining images of tumors after different treatments. The tumor-bearing mice that did not receive any treatment were defined as the BLK group. (b) Schematic illustration of the mechanism of NO-mediated autophagy inhibition.

faces the bottleneck of low heating performance of MNPs [9,10,71,88]. There are two main heating mechanisms of MNPs: hysteresis loss and relaxation loss [4,6]. Although most MNPs currently utilized including NanoTherm® are superparamagnetic nanoparticles that generate heat primarily based on the relaxation loss mechanism [54,55,60,62], ferromagnets with the hysteresis loss mechanism actually have more efficient heating performance at current MHT frequencies [10,63,64,88]. Therefore, ferrimagnetic $Zn_{0.5}Fe_{2.5}O_4$ nanocubes were synthesized, but due to their magnetism, $Zn_{0.5}Fe_{2.5}O_4$ MNPs were prone to aggregate in water (Fig. 4b), which greatly weakened their magnetic-heat conversion efficiency (Fig. 4a). Fortunately, the sol-gel transition process of our NO-Gel facilitated the homogeneous dispersion of MNPs at low temperatures and achieved the firm anchoring of MNPs after gelation (Fig. 4b), which not only boosted the magnetic-heat conversion efficiency of $Zn_{0.5}Fe_{2.5}O_4$ MNPs (Fig. 4a) but also provided the ability to perform multiple MHT after a single administration of MNPs@NO-Gel (Fig. 8). As a result, the ILP value of $Zn_{0.5}Fe_{2.5}O_4$ MNPs in NO-Gel reached 8.44 nH $m^2$/kg under a safe magnetic field for human MHT ($H$: 17.6 kA/m; $f$: 282 kHz) (Fig. 4c), which is significantly higher than that of commercial NanoTherm® (0.74–0.99 nH $m^2$/kg) [10], and also greatly diminished the amount of MNPs that need to be loaded into NO-Gel for MHT.

*In vitro* release tests confirmed that the MNPs@NO-Gel system could release NO continuously for a long time (Fig. 4e). More intriguingly, the release rate of NO could be accelerated *via* water bath or AMF-induced heating (Fig. 4f), which is conducive to enhancing MHT efficacy. The *in vivo* degradation of MNPs@NO-Gel lasted for more than one month after a single subcutaneous injection (Fig. 7a and b), and the degradation of NO-Gel governed the release of MNPs (Fig. 7c). Additionally, the released MNPs were mainly metabolized *via* the spleen (Fig. 7d).

Both *in vitro* cell experiments and *in vivo* antitumor results corroborated that the released NO from NO-gel could enhance the anticancer efficacy of mild hyperthermia (Fig. 5d and 9b). In particular, after a single injection of MNPs@NO-Gel at the tumor site plus subsequent three mild MHT, CT-26 tumors were thoroughly removed (Fig. 9b and h) without recurrence even on day 50 (Fig. S17). Meanwhile, this excellent antitumor efficacy of the MNPs@NO-Gel + MHT³ system not only arrested the occurrence of tumor-related complications, such as splenomegaly (Fig. 9e) and systemic inflammation response (Fig. 9f and g), but also did not cause any acute toxicity (Figs. S21–22) and systemic side-effects (Figs. S18–20).

Finally, based on our findings *in vitro* and *in vivo* combined with a previous study [17], we proposed and perfected the mechanism by which NO inhibited the mild hyperthermia-induced autophagy pathway, as illustrated in Fig. 10b. After tumor cells suffered from mild hyperthermia, the self-restoring autophagy pathway was provoked. Under normal conditions, autophagosomes encapsulating impaired proteins and organelles fuse with lysosomes to form autolysosomes. Then, these proteins and organelles are degraded by enzymes derived from lysosomes to generate nutrients such as amino acids and pyruvate to repair damaged cells [7]. However, NO can inhibit double membranes departing from endoplasmic reticulum to form phagophores [28], thereby blocking the formation of autophagosomes. This was proved by our study (Fig. 6f, h-i). Meanwhile, we found that lysosomes were also strongly destroyed by an adequate supply of NO (Fig. 6f and g), which arrested the fusion of autophagosomes and lysosomes to form autolysosomes, resulting in that impaired proteins and organelles could not be degraded for repairing damaged tumor cells. Collectively, the efficacy of mild MHT was dramatically strengthened. All in all, we revealed for the first time that autophagy inhibition mediated by an abundant supply of NO not only blocked autophagosome formation but also synchronously destroyed lysosomes, which contributes to further understanding of the mechanism of NO-mediated autophagy inhibition.

## 4. Conclusion

A novel injectable and thermosensitive NO-Gel containing abundant NO donors has been developed to enhance the antitumor efficacy of mild MHT. $Zn_{0.5}Fe_{2.5}O_4$ MNPs with high heating performance based on the hysteresis loss mechanism were also prepared. The aggregation of NO-micelles driven *via* hydrophobic interactions plus the dehydration of PEG upon heating is responsible for the formation of temperature-responsive NO-gel. The introduction of MNPs had no significant effects on the injectability of MNPs@NO-Gel, and the system still exhibited a sol-gel transition along with the elevation of temperature. More importantly, the MNPs@NO-Gel system was capable of performing multiple MHT and achieving precise heating with only one administration. This is attributed to the uniform distribution and firm fixation of MNPs in NO-Gel. Also, MNPs@NO-Gel could continuously release NO and MHT could expedite the release of NO. The *in vivo* maintenance of MNPs@NO-Gel exceeded one month and the released $Zn_{0.5}Fe_{2.5}O_4$ MNPs could be metabolized *via* the spleen. After injection of MNPs@NO-Gel into the tumor area, three mild MHT treatments with similar heating efficiency were conveniently achieved. The sustained and sufficient release of NO from NO-Gel drastically inhibited self-repairing autophagic flux induced by damaged tumor cells, thus evidently amplifying the antitumor effect of mild MHT. In consequence, CT-26 colon tumors were thoroughly eradicated without occurrence of recurrence and other systemic side-effects.

In addition, the injectable and NO-releasing hydrogel is suitable as a co-delivery vehicle for multifarious drugs and can be extended to various NO-related medical applications. The modification methodology based on PEG-polypeptide copolymers developed by us provides a valuable reference for designing other injectable hydrogels modified with a myriad of divergent active molecules or drugs.

## 5. Experimental section

### 5.1. Animals

The female BALB/c mice were provided by Shanghai Lab. Animal Research Center. The animals were raised in a suitable environment at 22–25 °C and had free access to water and food.

### 5.2. Synthesis of NO-polymer

Firstly, P(Ala-*co*-BLA)-PEG-P(Ala-*co*-BLA) triblock copolymers were synthesized *via* the ring-opening copolymerization of L-Ala-NCA and L-Asp(obzl)-NCA in the presence of $NH_2$-PEG-$NH_2$ as the macroinitiator and 18-C-6 as the catalyst. Briefly, L-Ala-NCA (2.76 g, 24 mmol), L-Asp(obzl)-NCA (3.49 g, 14 mmol) and 18-C-6 (528 mg, 2 mmol) were added into a 250 mL Schlenk flask and the flask was then filled with argon gas. Next, dried dichloromethane (DCM, 50 mL) and dimethyl formamide (DMF, 4 mL) were added to dissolve the raw materials, and 10 mL of DCM dissolved with $NH_2$-PEG-$NH_2$ (2 g, 1 mmol) was quickly injected into the flask. After 24 h of reaction, the solution was added into 1000 mL ice diethyl ether to isolate the product. After filtration and vacuum drying, P(Ala-*co*-BLA)-PEG-P(Ala-*co*-BLA) copolymers (6.15 g, 93.5 % yield) were obtained.

Subsequently, P(Ala-*co*-BLA)-PEG-P(Ala-*co*-BLA) (2 g, 0.31 mmol, containing 4.1 mmol benzyl ether groups) was dissolved into 40 mL anhydrous dimethyl sulfoxide (DMSO). After that, excess ETA (2.45 mL, 41 mmol) in 10 mL anhydrous DMSO was added and the system was agitated at 80 °C for 24 h under the protection of argon. Next, the reaction solution was added into diethyl ether at room temperature to precipitate the polymers. After filtration and lyophilization, P(Ala-*co*-Asp(ETA))-PEG-P(Ala-*co*-Asp(ETA)) copolymers (1.54 g, 85.1 % yield) were collected.

Finally, NO-polymer was obtained *via* modifying NEAA onto the side chains of P(Ala-*co*-Asp(ETA))-PEG-P(Ala-*co*-Asp(ETA)). Briefly, P(Ala-

co-Asp(ETA))-PEG-P(Ala-co-Asp(ETA)) (2 g, 0.34 mmol, containing 4.56 mmol hydroxyl groups) was dissolved in 30 mL of anhydrous DMSO. NEAA (1.13 g, 9.34 mmol), 3-(3-dimethylaminopropyl)-1-ethylcarbodiimide hydrochloride (EDC·HCl, 2.70 g, 14.07 mmol) and 4-dimethylaminopyridine (DMAP, 0.57 g, 4.69 mmol) were dissolved together in another 40 mL of DMSO, and then added dropwise to the above solution. Afterwards, the system was stirred at room temperature for 24 h. After the completion of the reaction, the crude NO-polymers were set apart *via* precipitation in diethyl ether at room temperature. After dialysis and lyophilization, the final product (1.62 g, 65.1 % yield) was attained.

### 5.3. Characterization of NEAA and various polymers

$^1$H NMR spectra of NEAA, OMs-PEG-OMs, NH$_2$-PEG-NH$_2$, mPEG-OMs and mPEG-NH$_2$ in CDCl$_3$, and P(Ala-co-BLA)-PEG-P(Ala-co-BLA), P(Ala-co-Asp(ETA))-PEG-P(Ala-co-Asp(ETA)), NO-polymer and BK-polymer in CF$_3$COOD were recorded on a proton NMR spectrometer (Bruker AVANCE III HD, 400 MHz) to verify their compositions. A GPC system (Agilent 1260) was employed to attain the MWs and molar mass dispersity ($Đ_M$) values of NH$_2$-PEG-NH$_2$, NO-polymer, mPEG-NH$_2$ and BK-polymer. The decoration degree of NEAA in NO-polymer was confirmed by a UV–vis spectrometer (TU-1950, Beijing Purkinje General Instrument Co. Ltd, China). In brief, the absorbance of NEAA aqueous solutions with various concentrations at 194 nm was detected to establish a standard curve. After that, the absorbance of aqueous solutions of NO-polymer and P(Ala-co-Asp(ETA))-PEG-P(Ala-co-Asp(ETA)) with the same concentration at 194 nm was also measured. According to the difference value ($A_{194, \text{NO}} − A_{194, \text{ETA}}$), the decoration degree of NEAA in NO-polymer was confirmed. $A_{194, \text{NO}}$ and $A_{194, \text{ETA}}$ denote the absorbance values of NO-polymer and P(Ala-co-Asp(ETA))-PEG-P(Ala-co-Asp(ETA)) solutions at 194 nm, respectively.

### 5.4. Synthesis and characterization of Zn$_{0.5}$Fe$_{2.5}$O$_4$ nanocubes

Zn$_{0.5}$Fe$_{2.5}$O$_4$ MNPs were synthesized according to previous reports [10,63,64]. Briefly, Fe(acac)$_3$ (0.79 g, 2.24 mmol), Zn(acac)$_2$ (0.59 g, 2.24 mmol), oleic acid (1.13 g, 4 mmol) and sodium oleate (0.5 g, 1.66 mmol) were added into a 100 mL three-neck flask containing 10 mL benzyl ether. Under an argon atmosphere, the mixture solution was heated to 290 °C within 20 min and then agitated with a thermal-resistance magnetic stir bar for 1 h. Next, the system was cooled down, and 50 mL ethanol was added to separate the crude product. Afterwards, the sediments were obtained through centrifugation at 5000 rpm for 5 min. The final product (190 mg, 89.6 % yield) was obtained by washing with CHCl$_3$ for three times and stored in toluene until use. The morphology of MNPs was scanned by TEM (Tecnai G2 20 TWIN, FEI). The constituents of MNPs were analyzed by an ICP-OES system (iCAP 7400, Thermofisher) and a SEM system equipped with an EDS system (Hitachi Regulus 8100). The XRD pattern of MNPs was obtained *via* a diffractometer (Rigaku Ultima IV). *M-H* behavior of MNPs at 300 K was recorded by a Physical Property Measurement System (Quantum Design, MPMS (SQUID) VSM).

### 5.5. Observation of micellar behaviors of different copolymers

Firstly, CD spectra of aqueous solutions of NO-polymer and BK-polymer at different concentrations were recorded *via* a CD spectroscopy (Chirascan, Applied Photophysics Ltd.). The wavelength of the minimum ellipticity in the CD spectra was plotted as a function of logarithmic polymer concentration. The crossing point of the two extrapolated lines was defined as CMC. The size and distribution of NO-micelles (0.1 wt%) and BK-micelles (0.1 wt%) at different temperatures were measured *via* a DLS apparatus (Zetasizer Nano, ZS90, Malvern). Meanwhile, the aqueous solutions of the two copolymers were dropped on the copper grids at 15 °C and 37 °C, respectively, and the

morphology of micelles was then observed *via* TEM.

### 5.6. Dynamic rheological measurement

The rheological properties of NO-Gel and BK-Gel with or without MNPs were measured *via* a dynamic rheometer (Kinexus, Malvern) installed with a cone plate (60 mm diameter, 1° angle and 0.03 mm gap) in a temperature sweep mode. 2 mL solution was dropped on the basal plate. The temperature increased from 10 °C to 45 °C at a rate of 1 °C/min and the oscillation frequency was set to1.592 Hz.

### 5.7. Measurement of heating efficacy of MNPs

The heating curves of MNPs dispersed in chloroform, NO-Gel, and water were recorded on the MAGNETIC HYPERTHERMIA SYSTEM (MSI Automation INC.). The *H* and *f* were set at 46.6 kA/m and 300 kHz, respectively, or 17.6 kA/m and 282 kHz, respectively. The SLP and ILP values were obtained using the following equations:

$$\text{SLP} = \frac{C \times m}{m_{\text{MNPs}}} \times \frac{dT}{dt} \tag{1}$$

$$\text{ILP} = \frac{\text{SLP}}{H^2 \times f} \tag{2}$$

where *C* is the specific heat capacity of the solvent, *m* is the mass of the solvent, $m_{\text{MNPs}}$ is the mass of MNPs in solution, and $dT/dt$ is the slope of the temperature-raising curve at the initial stage.

### 5.8. In vitro release of MNPs and NO

0.5 mL MNPs@NO-Gel solution was added into a 10 mL glass vial (inner diameter: 10 mm) and transferred to a 37 °C shaking bath. After the formation of an *in situ* hydrogel, 5 mL phosphate buffer saline (PBS) solution was added. 4 mL supernatant was taken out and replaced by 4 mL new PBS at each sampling time. The release amount of MNPs was measured *via* ICP-OES, while the release amount of NO was analyzed *via* the Griess assay kit.

Meanwhile, 0.5 mL MNPs@NO-Gel solution was added to a 5 mL centrifuge tube and put into a shaking bath at 37 °C or 43 °C. After the formation of an *in situ* hydrogel, 4 mL PBS containing 50 μM DAF-FM was added. In addition, the hydrogel was also heated to 43 °C with AMF and then 4 mL PBS containing DAF-FM was added. DAF-FM was obtained *via* NaOH-mediated hydrolyzation of DAF-FM DA. After heating for 30 min, the fluorescence emission spectra of supernatants were obtained with a fluorescence spectrophotometer (QM40, PTI) under the excitation of 495 nm.

### 5.9. Intracellular NO observation

CT-26 cells were sowed on glass bottom dishes ($2 \times 10^5$/dish) and cultured overnight. Then, the cells were incubated with a new medium encapsulating 1000 μg/mL BK-micelles or NO-micelles for 4 h. To simulate MHT and evaluate the influence of heating on the intracellular release of NO, the cells treated with NO-micelles were immediately placed in a $42.5 \pm 0.5$ °C water bath for 20 min and then incubated at 37 °C for another 220 min (the NO-micelles + heat group). Afterwards, the cells were co-cultured with RPMI 1640 containing 2.5 μM DAF-FM DA (without fetal bovine serum (FBS) and phenol red) for 30 min. After being fixed with 4 wt% paraformaldehyde and stained with DAPI, the cells were observed by CLSM (C2+, Nikon) under FITC and DAPI channels. The cells stained with DAF-FM DA but not fixed were analyzed in the FL1 channel of a flow cytometer (Gallios, Beckman Coulter).

## 5.10. Antitumor evaluation in vitro

CT-26 cells were sowed on 96-well plates ($4 \times 10^3$/well) and cultured overnight. After that, the cells were incubated with 200 μL of fresh medium containing BK-polymer, NO-polymer, MNPs@BK-polymer, or MNPs@NO-polymer at different concentrations for 24 h. The ratio of copolymers to MNPs was fixed at 100:3. For the simulated multiple MHT groups, such as the MNPs@BK-polymer + heat$^3$ and MNPs@NO-polymer + heat$^3$ groups, the cells treated with MNPs@BK-polymer or MNPs@NO-polymer were immediately cultured in a 42.5 ± 0.5 °C water bath for 20 min and then incubated at 37 °C for another 100 min. Next, the cells received the second and third hyperthermia 2 and 4 h after treatment. After the completion of the three circles, the cells were further cultivated at 37 °C for another 20 h. Finally, the cell viability was assessed *via* the CCK-8 assay. The cell viability in the control group treated only with cell medium was set as 100 %.

To investigate the anticancer mechanism of hyperthermia groups, 5 mM autophagy inhibitor 3-MA was added into MNPs@BK-micelles and 200 nM autophagy inducer Rapa was added into MNPs@NO-micelles. After various treatments, the cell viability was also evaluated.

## 5.11. Western blot assay

To analyze the expression of LC3B protein, CT-26 cells were seeded on 6-well plates ($6 \times 10^5$/well) and cultured overnight. Then, the cells were incubated with 1000 μL of fresh medium containing BK-micelles, NO-micelles, MNPs@BK-micelles, or MNPs@NO-micelles for 4 h plus 50 min. The concentrations of copolymers and MNPs were 1000 μg/mL and 30 μg/mL, respectively. For the MNPs@BK-micelles + heat and MNPs@NO-micelles + heat groups, the cells were first cultivated with MNPs@BK-micelles or MNPs@NO-micelles at 37 °C for 4 h, and then put into a 42.5 ± 0.5 °C water bath for 20 min, and finally cultured at 37 °C for another 30 min. Next, the cells were lysed and the protein was harvested and quantified by the BCA kit. After being mixed with SDS loading buffer and boiled for 5 min, the protein was separated by 15 % SDS-PAGE and transferred onto nitrocellulose (NC) membranes. Afterwards, the NC membranes were blocked in Protein Free Rapid Blocking Buffer (Shanghai Epizyme Biomedical Technology Co., Ltd) for 15 min and incubated with rabbit anti-LC3B (Abcam, 1:2000) and rabbit anti-β-actin (Beyotime, 1:1000) at 4 °C overnight. Then, the membranes were washed three times and incubated with a chemiluminescent secondary antibody for 1 h. Finally, the membranes were washed three times and visualized *via* a chemiluminescent imaging system (Odyssey Fc, LI-COR).

The expression of p62 protein was assessed by an automated capillary Western blot system (Bio-Techne, USA). According to the manufacturer's protocol, the collected protein was denatured and added into a 12–230 kDa assay plate with 25 capillaries (SM-004, Bio-Techne). Then, the protein was separated in capillaries at 375 V. After that, antibody diluent containing rabbit anti-p62 (Beyotime, 1:50) and anti-β-actin (1:50), horseradish peroxidase (HRP) conjugated secondary antibody solution, and luminescent solution consisting of luminol-S and peroxide were successively run in the capillaries. Finally, the chemiluminescence intensity was measured and the areas under the chemiluminescence intensity curves were calculated using the software Compass for SW (Bio-Techne) to determine protein levels.

## 5.12. Autophagy detection

CT-26 cells were sowed on glass bottom dishes ($2 \times 10^5$/dish) and cultured overnight. Then, the cells were incubated with 1000 μL of new medium encapsulating 1000 μg BK-micelles or NO-micelles for 4 h plus 50 min. For the BK-micelles + heat and NO-micelles + heat groups, the cells were first cultured at 37 °C for 4 h, then in a water bath at 42.5 ± 0.5 °C for 20 min, and finally at 37 °C for 30 min. Afterwards, the cells were incubated with RPMI 1640 (with 5 % FBS and without phenol red)

containing CYTO-ID (1:1000) and Lysotracker red (50 nM) for 30 min. After being fixed with 4 wt% paraformaldehyde and stained with DAPI, the cells were imaged by CLSM under FITC, TRITC and DAPI channels. The cells stained with CYTO-ID but not fixed were also detected in the FL1 channel of a flow cytometer.

## 5.13. In vivo degradation and metabolism

To investigate the degradation behavior of NO-Gel *in vivo*, 0.1 mL NO-Gel loaded with RB-PA-PEG-RB-PA (0.35 mg/mL) was injected subcutaneously into the back of BALB/c mice. Afer that, an optical and X-ray small animal imaging system (In Vivo Xtreme, Bruker) was used to monitor the *in vivo* degradation of NO-Gel.

The *in vivo* degradation behavior of MNPs@NO-Gel was also assessed. 0.1 mL MNPs@NO-Gel was injected subcutaneously into the back of BALB/c mice and some mice were sacrificed and dissected at each predetermined time point. Then, the residual hydrogels were isolated and weighed. After dissolving the residual hydrogel in 10 wt% HCl solution, the remnant amount of MNPs in filtrate was confirmed *via* ICP-OES. In addition, the main organs were also collected, fixed with 4 wt% paraformaldehyde, sliced and stained with Prussian blue to detect *in vivo* distribution of iron(III) ions.

## 5.14. In vivo antitumor efficacy

BALB/c mice received hypodermic innoculation of $1 \times 10^6$ CT-26 cells on the right flank of the dorsal region. When tumors reached about 100 mm$^3$, all animals were arbitrarily allocated into 6 groups (7 mice per group): 1) BLK, 2) MNPs@BK-Gel, 3) NO-Gel, 4) MNPs@NO-gel, 5) MNPs@BK-Gel + MHT$^3$, and 6) MNPs@NO-gel + MHT$^3$. For the group 1, the mice were not subject to any therapy. For the groups 2–4, the mice were intratumorally injected with 0.05 mL hydrogel coupled with peritumoral injection of 0.15 mL hydrogel. For the groups 5–6, after different interventions, the animals were treated with MHT three times on day 0, day 2 and day 4. The *H* and *f* were set at 17.6 kA/m and 282 kHz, respectively. For each MHT, the temperature of tumors was maintained at 42.5 ± 1.0 °C for 20 min, and the tumor region was monitored and recorded by an infrared thermal camera. The tumor size was calculated based on the formula $V = a \times b^2/2$, where $V$ is the tumor volume, $a$ is the longest diameter of the tumor and $b$ is the shortest diameter of the tumor. The tumor size and body weight were measured and recorded every two days. On day 14, one mouse was sacrificed at random in each group and the tumors were harvested, fixed with 4 wt% paraformaldehyde, sliced and stained with TUNEL and H&E. The main organs were also collected and stained with H&E. The other mice were observed until death. When the tumor grew over 2000 mm$^3$, the mouse was regarded dead and euthanized. Once the mice were euthanized, the collected spleens were weighed, and the whole blood and serum specimens were extracted to assess blood routine indexes and liver and renal functions, respectively. The survival mice were sacrificed on day 50 and the above procedures were then conducted.

Moreover, when some tumors grew to 100 mm$^3$, the mice received MNPs@BK-Gel or MNPs@NO-Gel treatment plus once MHT. On the next day, the tumors were harvested and conducted with LC3B-II and p62 immunofluorescence staining.

## 5.15. Statistical analysis

The significant difference was analyzed *via* one-way ANOVA with the setting of "*" when $p < 0.05$, "**" when $p < 0.01$, "***" when $p < 0.001$. All data for statistical analysis were displayed as mean ± SEM.

## Ethics approval and consent to participate

All animal experiments were approved by the Ethics Committee of Fudan University (202101006S).

## CRediT authorship contribution statement

**Yaoben Wang:** Writing – original draft, Methodology, Investigation, Formal analysis, Data curation, Conceptualization. **Xiaobin Chen:** Writing – review & editing, Methodology. **Zhiyong Chen:** Writing – review & editing, Methodology. **Xin Wang:** Writing – review & editing, Methodology. **Hancheng Wang:** Writing – review & editing. **Huajuan Zhai:** Writing – review & editing. **Jiandong Ding:** Writing – review & editing, Resources, Funding acquisition. **Lin Yu:** Writing – original draft, Supervision, Resources, Funding acquisition, Conceptualization.

## Declaration of competing interest

The authors declare no competing interests.

## Acknowledgements

## Appendix B. Supplementary data

Supplementary data to this article can be found online at https://doi. org/10.1016/j.bioactmat.2024.05.032.

## References

[1] M.Y. Chang, Z.Y. Hou, M. Wang, C.X. Li, J. Lin, Recent advances in hyperthermia therapy-based synergistic immunotherapy, Adv. Mater. 33 (4) (2021) 2004788.

[2] G. Hannon, F.L. Tansi, I. Hilger, A. Prina-Mello, The effects of localized heat on the hallmarks of cancer, Adv. Ther. 4 (7) (2021) 2000267.

[3] J. Beik, Z. Abed, F.S. Ghoreishi, S. Hosseini-Nami, S. Mehrzadi, A. Shakeri-Zadeh, S.K. Kamrava, Nanotechnology in hyperthermia cancer therapy: from fundamental principles to advanced applications, J. Contr. Release 235 (2016) 205–221.

[4] S.K. Sharma, N. Shrivastava, F. Rossi, L.D. Tung, N.T.K. Thanh, Nanoparticles-based magnetic and photo induced hyperthermia for cancer treatment, Nano Today 29 (2019) 100795.

[5] D.G. Zhang, W.Z. Li, Y.X. Shang, L.R. Shang, Programmable microfluidic manipulations for biomedical applications, Eng. Regen. 3 (3) (2022) 258–261.

[6] X.L. Liu, Y.F. Zhang, Y.Y. Wang, W.J. Zhu, G.L. Li, X.W. Ma, Y.H. Zhang, S.Z. Chen, S. Tiwari, K.J. Shi, S.W. Zhang, H.M. Fan, Y.X. Zhao, X.J. Liang, Comprehensive understanding of magnetic hyperthermia for improving antitumor therapeutic efficacy, Theranostics 10 (8) (2020) 3793–3815.

[7] M. Wang, Q. Chen, D. Xu, Z.B. Yang, J.F. Chen, Y. Zhang, H.R. Chen, Self-cycling redox nanoplatform in synergy with mild magnetothermal and autophagy inhibition for efficient cancer therapy, Nano Today 43 (2022) 101374.

[8] X. Lin, L.J. Cai, X.Y. Cao, Y.J. Zhao, Stimuli-responsive silk fibroin for on-demand drug delivery, Smart Med 2 (2) (2023) e20220019.

[9] K. Maier-Hauff, F. Ulrich, D. Nestler, H. Niehoff, P. Wust, B. Thiesen, H. Orawa, V. Budach, A. Jordan, Efficacy and safety of intratumoral thermotherapy using magnetic iron-oxide nanoparticles combined with external beam radiotherapy on patients with recurrent glioblastoma multiforme, J. Neuro Oncol. 103 (2) (2011) 317–324.

[10] X.B. Chen, H.C. Wang, J.Y. Shi, Z.Y. Chen, Y.B. Wang, S.Y. Gu, Y. Fu, J.L. Huang, J. D. Ding, L. Yu, An injectable and active hydrogel induces mutually enhanced mild magnetic hyperthermia and ferroptosis, Biomaterials 298 (2023) 122139.

[11] J. Ge, N.L. Yang, Y.Q. Yang, H. Yu, X.Y. Yang, Y.J. Wang, T.Y. Wang, Y.S. Cheng, Y. J. Wang, Z.H. Han, Y. Teng, J. Zou, H.L. Yang, L. Cheng, The combination of eddy thermal effect of biodegradable magnesium with immune checkpoint blockade shows enhanced efficacy against osteosarcoma, Bioact. Mater. 25 (2023) 73–85.

[12] N.L. Yang, X.W. Sun, Y.K. Zhou, X.Y. Yang, J.X. You, Z.P. Yu, J. Ge, F. Gong, Z. S. Xiao, Y. Jin, Z. Liu, L. Cheng, Liquid metal microspheres with an eddy-thermal effect for magnetic hyperthermia-enhanced cancer embolization-immunotherapy, Sci. Bull. 68 (16) (2023) 1772–1783.

[13] X. Zhang, J.F. Du, Z. Guo, J. Yu, Q. Gao, W.Y. Yin, S. Zhu, Z.J. Gu, Y.L. Zhao, Efficient near infrared light triggered nitric oxide release nanocomposites for sensitizing mild photothermal therapy, Adv. Sci. 6 (3) (2019) 1801122.

[14] G. Gao, X.B. Sun, G.L. Liang, Nanoagent-promoted mild-temperature photothermal therapy for cancer treatment, Adv. Funct. Mater. 31 (25) (2021) 2100738.

[15] G. Gao, Y.W. Jiang, Y.X. Guo, H.R. Jia, X.T. Cheng, Y. Deng, X.W. Yu, Y.X. Zhu, H. Y. Guo, W. Sun, X.Y. Liu, J. Zhao, S.H. Yang, Z.W. Yu, F.M.S. Raya, G.L. Liang, F. G. Wu, Enzyme-mediated tumor starvation and phototherapy enhance mild-temperature photothermal therapy, Adv. Funct. Mater. 30 (16) (2020) 1909391.

[16] Z.J. Zhou, Y. Yan, K.W. Hu, Y. Zou, Y.W. Li, R. Ma, Q. Zhang, Y.Y. Cheng, Autophagy inhibition enabled efficient photothermal therapy at a mild temperature, Biomaterials 141 (2017) 116–124.

[17] M. Pérez-Hernández, A. Arias, D. Martínez-García, R. Pérez-Tomás, R. Quesada, V. Soto-Cerrato, Targeting autophagy for cancer treatment and tumor chemosensitization, Cancers 11 (10) (2019) 1599.

[18] T. Chen, D. Cen, Z.H. Ren, Y.F. Wang, X.J. Cai, J. Huang, L. Di Silvio, X. Li, G. R. Han, Bismuth embedded silica nanoparticles loaded with autophagy suppressant to promote photothermal therapy, Biomaterials 221 (2019) 119419.

[19] G. Gao, X.B. Sun, X.Y. Liu, Y.W. Jiang, R.Q. Tang, Y.X. Guo, F.G. Wu, G.L. Liang, Intracellular nanoparticle formation and hydroxychloroquine release for autophagy-inhibited mild-temperature photothermal therapy for tumors, Adv. Funct. Mater. 31 (34) (2021) 2102832.

[20] Z.Z. Zhou, Y. Liu, W.J. Li, Z.J. Zhao, X.W. Xia, J.L. Liu, Y.G. Deng, Y.B. Wu, X. Q. Pan, F. He, H.L. Yang, W.H. Lu, Y. Xu, X.S. Zhu, A self-adaptive biomimetic periosteum employing nitric oxide release for augmenting angiogenesis in bone defect regeneration, Adv. Healthcare Mater. 13 (3) (2023) 2302153.

[21] D.S. Zhu, J.L. Hou, M. Qian, D.W. Jin, T. Hao, Y.J. Pan, H. Wang, S.T. Wu, S. Liu, F. Wang, L.P. Wu, Y.M. Zhong, Z.L. Yang, Y.Z. Che, J. Shen, D.L. Kong, M. Yin, Q. Zhao, Nitrate-functionalized patch confers cardioprotection and improves heart repair after myocardial infarction via local nitric oxide delivery, Nat. Commun. 12 (1) (2021) 4501.

[22] H. Xing, H. Peng, Y. Yang, K. Lv, S. Zhou, X. Pan, J. Wang, Y. Hu, G. Li, D. Ma, Nitric oxide synergizes minoxidil delivered by transdermal hyaluronic acid liposomes for multimodal androgenetic-alopecia therapy, Bioact. Mater. 32 (2024) 190–205.

[23] V.G. Deepagan, H. Ko, S. Kwon, N.V. Rao, S.K. Kim, W. Um, S. Lee, J. Min, J. Lee, K.Y. Choi, S. Shin, M. Suh, J.H. Park, Intracellularly activatable nanovasodilators to enhance passive cancer targeting regime, Nano Lett. 18 (4) (2018) 2637–2644.

[24] Y. Liu, L. Cui, X. Wang, W.L. Miao, Y.X. Ju, T.D. Chen, H.T. Xu, N. Gu, F. Yang, In situ nitric oxide gas nanogenerator reprograms glioma immunosuppressive microenvironment, Adv. Sci. 10 (18) (2023) 2300679.

[25] D.F. Hu, Y.Y. Deng, F. Jia, Q. Jin, J. Ji, Surface charge switchable supramolecular nanocarriers for nitric oxide synergistic photodynamic eradication of biofilms, ACS Nano 14 (1) (2020) 347–359.

[26] A.C. Midgley, Y.Z. Wei, Z.J. Li, D.L. Kong, Q. Zhao, Nitric-oxide-releasing biomaterial regulation of the stem cell microenvironment in regenerative medicine, Adv. Mater. 32 (3) (2020) 1805818.

[27] Z.K. Jin, Y.Y. Wen, Y.X. Hu, W.W. Chen, X.F. Zheng, W.S. Guo, T.F. Wang, Z. Y. Qian, B.L. Su, Q.J. He, MRI-guided and ultrasound-triggered release of NO by advanced nanomedicine, Nanoscale 9 (10) (2017) 3637–3645.

[28] S. Sarkar, Viktor I. Korolchuk, M. Renna, S. Imarisio, A. Fleming, A. Williams, M. Garcia-Arencibia, C. Rose, S. Luo, Benjamin R. Underwood, G. Kroemer, Cahir J. O'Kane, David C. Rubinsztein, Complex inhibitory effects of nitric oxide on autophagy, Mol. Cell 43 (1) (2011) 19–32.

[29] Z.R. Zhou, Z.M. Gao, W. Chen, X.Z. Wang, Z.K. Chen, Z.C. Zheng, Q.Y. Chen, M. L. Tan, D.L. Liu, Y.R. Zhang, Z.Y. Hou, Nitric oxide-mediated regulation of mitochondrial protective autophagy for enhanced chemodynamic therapy based on mesoporous Mo-doped $Cu_9S_5$ nanozymes, Acta Biomater. 151 (2022) 600–612.

[30] X.Y. Liang, Y.H. Ji, Y. Zhou, S.Y. Wang, L. Binh Vong, N. Li, A "pursuit and interception" strategy of amplified autophagy inhibition for tumor therapy based on ultra-small Rh nanoparticles, Chem. Eng. J. 443 (2022) 136379.

[31] L.D. Jiang, D.Y. Chen, Z.K. Jin, C. Xia, Q.Q. Xu, M.J. Fan, Y.L. Dai, J. Liu, Y.P. Li, Q. J. He, Light-triggered nitric oxide release and structure transformation of peptide for enhanced intratumoral retention and sensitized photodynamic therapy, Bioact. Mater. 12 (2022) 303–313.

[32] H.T. Hu, D. Li, W.B. Dai, Q. Jin, D. Wang, J. Ji, B.Z. Tang, Z. Tang, A NIR-II AIEgen-based supramolecular nanodot for peroxynitrite-potentiated mild-temperature photothermal therapy of hepatocellular carcinoma, Adv. Funct. Mater. 33 (19) (2023) 2213134.

[33] Y.S. Wang, T. Yang, Q.J. He, Strategies for engineering advanced nanomedicines for gas therapy of cancer, Natl. Sci. Rev. 7 (9) (2020) 1485–1512.

[34] Y.Y. Deng, Y.P. Wang, F. Jia, W.F. Liu, D.F. Zhou, Q. Jin, J. Ji, Tailoring supramolecular prodrug nanoassemblies for reactive nitrogen species-potentiated chemotherapy of liver cancer, ACS Nano 15 (5) (2021) 8663–8675.

[35] J. Zou, Z. Li, Y. Zhu, Y. Tao, Q. You, F. Cao, Q. Wu, M. Wu, J. Cheng, J. Zhu, X. Chen, pH/GSH dual responsive nanosystem for nitric oxide generation enhanced type I photodynamic therapy, Bioact. Mater. 34 (2024) 414–421.

[36] H. Ma, Y. Tang, F. Rong, K. Wang, T. Wang, P. Li, Surface charge adaptive nitric oxide nanogenerator for enhanced photothermal eradication of drug-resistant biofilm infections, Bioact. Mater. 27 (2023) 154–167.

[37] Y.H. Hu, T. Lv, Y. Ma, J.J. Xu, Y.H. Zhang, Y.L. Hou, Z.J. Huang, Y. Ding, Nanoscale coordination polymers for synergistic NO and chemodynamic therapy of liver cancer, Nano Lett. 19 (4) (2019) 2731–2738.

[38] J.Y. Shi, L. Yu, J.D. Ding, PEG-based thermosensitive and biodegradable hydrogels, Acta Biomater. 128 (2021) 42–59.

[39] D.L.G. Cao, J.D. Ding, Recent advances in regenerative biomaterials, Regen. Biomater. 9 (2022) rbac098.

[40] D. Zhao, Y. Rong, D. Li, C.L. He, X.S. Chen, Thermo-induced physically crosslinked polypeptide-based block copolymer hydrogels for biomedical applications, Regen. Biomater. 10 (2023) rbad039.

[41] S.Y. Gu, H.C. Wang, Y.B. Wang, X. Wang, X. Liu, Y. Wang, P. Liu, J.D. Ding, L. Yu, Thermosensitive nanocomposite hydrogel composed of PVPylated poly(D,L-alanine) and laponite as an injectable and bioactive biomaterial, Chem. Eng. J. 466 (2023) 143128.

[42] Y. Li, L. Li, M. Wang, B. Yang, B. Huang, S. Bai, X. Zhang, N. Hou, H. Wang, Z. Yang, C. Tang, Y. Li, W. Yuk-Wai Lee, L. Feng, M.D. Tortorella, G. Li, O-alg-THAM/gel hydrogels functionalized with engineered microspheres based on

mesenchymal stem cell secretion recruit endogenous stem cells for cartilage repair, Bioact. Mater. 28 (2023) 255–272.

[43] D.L.G. Cao, X. Chen, F. Cao, W. Guo, J.Y. Tang, C.Y. Cai, S.Q. Cui, X.W. Yang, L. Yu, Y. Su, J.D. Ding, An intelligent transdermal formulation of ALA-loaded copolymer thermogel with spontaneous asymmetry by using temperature-induced sol–gel transition and gel–sol (suspension) transition on different sides, Adv. Funct. Mater. 31 (22) (2021) 2100349.

[44] X.H. Wu, X. Wang, X.B. Chen, X.W. Yang, Q. Ma, G.H. Xu, L. Yu, J.D. Ding, Injectable and thermosensitive hydrogels mediating a universal macromolecular contrast agent with radiopacity for noninvasive imaging of deep tissues, Bioact. Mater. 6 (12) (2021) 4717–4728.

[45] J.N. Li, L. Li, T.K. Wu, K. Shi, Z.W. Bei, M. Wang, B.Y. Chu, K.Q. Xu, M. Pan, Y.C. Li, X.L. Hu, L.H. Zhang, Y. Qu, Z.Y. Qian, An injectable thermosensitive hydrogel containing resveratrol and dexamethasone-loaded carbonated hydroxyapatite microspheres for the regeneration of osteoporotic bone defects, Small Methods (2023) 2300843.

[46] C.Y. Wang, N.B. Feng, F. Chang, J.C. Wang, B.M. Yuan, Y.L. Cheng, H. Liu, J.K. Yu, J. Zou, J.X. Ding, X.S. Chen, Injectable cholesterol-enhanced stereocomplex polylactide thermogel loading chondrocytes for optimized cartilage regeneration, Adv. Healthcare Mater. 8 (14) (2019) 1900312.

[47] B. Zhao, Y. Zhuang, Z. Liu, J. Mao, S. Qian, Q. Zhao, B. Lu, X. Mao, L. Zhang, Y. Zhang, W. Cui, X. Sun, Regulated extravascular microenvironment via reversible thermosensitive hydrogel for inhibiting calcium influx and vasospasm, Bioact. Mater. 21 (2023) 422–435.

[48] W. Chen, K. Shi, J. Liu, P.P. Yang, R.X. Han, M. Pan, L.P. Yuan, C. Fang, Y.Y. Yu, Z. Y. Qian, Sustained co-delivery of 5-fluorouracil and cis-platinum via biodegradable thermo-sensitive hydrogel for intraoperative synergistic combination chemotherapy of gastric cancer, Bioact. Mater. 23 (2023) 1–15.

[49] J.J. Deng, X. Wang, W.H. Zhang, L.Y. Sun, X.X. Han, X.Q. Tong, L.M. Yu, J.D. Ding, L. Yu, Y.H. Liu, Versatile hypoxic extracellular vesicles laden in an injectable and bioactive hydrogel for accelerated bone regeneration, Adv. Funct. Mater. 33 (21) (2023) 2211664.

[50] Y.J. Woo, M. Patel, H. Kim, J.K. Park, Y.J. Jung, S.S. Cha, B. Jeong, Pralatrexate sustainably released from polypeptide thermogel is effective for chondrogenic differentiation of mesenchymal stem cells, ACS Appl. Mater. Interfaces 14 (3) (2022) 3773–3783.

[51] Z.Q. Lin, J.F. Ding, X.S. Chen, C.L. He, pH- and temperature-responsive hydrogels based on tertiary amine-modified polypeptides for stimuli-responsive drug delivery, Chem. Asian J. 18 (8) (2023) e202300021.

[52] Y. Cao, Y.H. Zhou, Z.X. Chen, Z. Zhang, X.S. Chen, C.L. He, Localized chemotherapy based on injectable hydrogel boosts the antitumor activity of adoptively transferred T lymphocytes in vivo, Adv. Healthcare Mater. 10 (19) (2021) 2100814.

[53] Y. Jeong, M.K. Joo, K.H. Bahk, Y.Y. Choi, H.T. Kim, W.K. Kim, H. Jeong Lee, Y. S. Sohn, B. Jeong, Enzymatically degradable temperature-sensitive polypeptide as a new in-situ gelling biomaterial, J. Contr. Release 137 (1) (2009) 25–30.

[54] Z.Q. Zhang, S.C. Song, Thermosensitive/superparamagnetic iron oxide nanoparticle-loaded nanocapsule hydrogels for multiple cancer hyperthermia, Biomaterials 106 (2016) 13–23.

[55] Z.Q. Zhang, S.C. Song, Multiple hyperthermia-mediated release of TRAIL/SPION nanocomplex from thermosensitive polymeric hydrogels for combination cancer therapy, Biomaterials 132 (2017) 16–27.

[56] B.B. Seo, Y.J. Kwon, J. Kim, K.H. Hong, S.E. Kim, H.R. Song, Y.M. Kim, S.C. Song, Injectable polymeric nanoparticle hydrogel system for long-term anti-inflammatory effect to treat osteoarthritis, Bioact. Mater. 7 (2022) 14–25.

[57] Y.B. Wang, X.W. Yang, X.B. Chen, X. Wang, Y. Wang, H.C. Wang, Z.Y. Chen, D.L. G. Cao, L. Yu, J.D. Ding, Sustained release of nitric oxide and cascade generation of reactive nitrogen/oxygen species via an injectable hydrogel for tumor synergistic therapy, Adv. Funct. Mater. 32 (36) (2022) 2206554.

[58] Z.Y. Piao, J.K. Park, B. Jeong, Cytogel: a cell-crosslinked thermogel, ACS Appl. Mater. Interfaces 15 (14) (2023) 17688–17695.

[59] L.B. Vong, T.Q. Bui, T. Tomita, H. Sakamoto, Y. Hiramatsu, Y. Nagasaki, Novel angiogenesis therapeutics by redox injectable hydrogel - regulation of local nitric oxide generation for effective cardiovascular therapy, Biomaterials 167 (2018) 143–152.

[60] H.A. Wu, L. Liu, L.N. Song, M. Ma, N. Gu, Y. Zhang, Enhanced tumor synergistic therapy by injectable magnetic hydrogel mediated generation of hyperthermia and highly toxic reactive oxygen species, ACS Nano 13 (12) (2019) 14013–14023.

[61] H.A. Wu, L.N. Song, L. Chen, Y.X. Huang, Y. Wu, F.C. Zang, Y.L. An, H.B. Lyu, M. Ma, J. Chen, N. Gu, Y. Zhang, Injectable thermosensitive magnetic nanoemulsion hydrogel for multimodal-imaging-guided accurate thermoablative cancer therapy, Nanoscale 9 (42) (2017) 16175–16182.

[62] K.Y. Qian, Y.H. Song, X. Yan, L. Dong, J.Z. Xue, Y.J. Xu, B. Wang, B.Q. Cao, Q. B. Hou, W. Peng, J.L. Hu, K. Jiang, S. Chen, H.Q. Wang, Y. Lu, Injectable ferrimagnetic silk fibroin hydrogel for magnetic hyperthermia ablation of deep tumor, Biomaterials 259 (2020) 120299.

[63] S.H. Noh, W. Na, J.T. Jang, J.H. Lee, E.J. Lee, S.H. Moon, Y.J. Lim, J.S. Shin, J. Cheon, Nanoscale magnetism control via surface and exchange anisotropy for optimized ferrimagnetic hysteresis, Nano Lett. 12 (7) (2012) 3716–3721.

[64] S.L. He, H.W. Zhang, Y.H. Liu, F. Sun, X. Yu, X.Y. Li, L. Zhang, L.C. Wang, K.Y. Mao, G.S. Wang, Y.J. Lin, Z.C. Han, R. Sabirianov, H. Zeng, Maximizing specific loss power for magnetic hyperthermia by hard–soft mixed ferrites, Small 14 (29) (2018) 1800135.

[65] Y.C. Xia, Z.Y. Song, Z.Z. Tan, T.R. Xue, S.Q. Wei, L.Y. Zhu, Y.F. Yang, H.L. Fu, Y. J. Jiang, Y. Lin, Y.B. Lu, A.L. Ferguson, J.J. Cheng, Accelerated polymerization of N-carboxyanhydrides catalyzed by crown ether, Nat. Commun. 12 (1) (2021) 732.

[66] U.P. Shinde, M.K. Joo, H.J. Moon, B. Jeong, Sol–gel transition of PEG–PAF aqueous solution and its application for hGH sustained release, J. Mater. Chem. 22 (13) (2012) 6072–6079.

[67] Y.M. Wei, S.Q. Cui, L. Yu, J.D. Ding, Degradation-influenced/induced self-assembly of copolymers with the combinatory effects of changed molecular weight and dispersity, Macromolecules 56 (7) (2023) 2619–2636.

[68] E.Y. Kang, B. Yeon, H.J. Moon, B. Jeong, PEG-$_{\text{L}}$-PAF and PEG-$_{\text{D}}$-PAF: comparative study on thermogelation and biodegradation, Macromolecules 45 (4) (2012) 2007–2013.

[69] S.Q. Cui, L. Yu, J.D. Ding, Semi-bald micelles and corresponding percolated micelle networks of thermogels, Macromolecules 51 (16) (2018) 6405–6420.

[70] A. Hervault, N.T.K. Thanh, Magnetic nanoparticle-based therapeutic agents for thermo-chemotherapy treatment of cancer, Nanoscale 6 (20) (2014) 11553–11573.

[71] X. Yu, Y. Mi, L.C. Wang, Z.R. Li, D.A. Wu, R.S. Liu, S.L. He, Effects of dipolar interactions on the magnetic hyperthermia of $Zn_{0.3}Fe_{2.7}O_4$ nanoparticles with different sizes, Chin. Phys. B 30 (1) (2021) 017503.

[72] C. Martinez-Boubeta, K. Simeonidis, D. Serantes, I. Conde-Leborán, I. Kazakis, G. Stefanou, L. Peña, R. Galceran, L. Balcells, C. Monty, D. Baldomir, M. Mitrakas, M. Angelakeris, Adjustable hyperthermia response of self-assembled ferromagnetic Fe-MgO core–shell nanoparticles by tuning dipole–dipole interactions, Adv. Funct. Mater. 22 (17) (2012) 3737–3744.

[73] G. Wang, Y.S. Feng, C.Y. Gao, X. Zhang, Q.S. Wang, J. Zhang, H.J. Zhang, Y.Q. Wu, X. Li, L. Wang, Y. Fu, X.Y. Yu, D.Y. Zhang, J.X. Liu, J.D. Ding, Biaxial stretching of polytetrafluoroethylene in industrial scale to fabricate medical ePTFE membrane with node-fibril microstructure, Regen. Biomater. 10 (2023) rbad056.

[74] Q.S. Wang, Q.S. Liu, J.M. Gao, J.H. He, H.J. Zhang, J.D. Ding, Stereo coverage and overall stiffness of biomaterial arrays underly parts of topography effects on cell adhesion, ACS Appl. Mater. Interfaces 15 (4) (2023) 6142–6155.

[75] D.K. Shi, Y.H. Kang, Z.L. Jiang, X. Li, H.J. Zhang, Q.S. Wang, J.Z. Guo, H.Y. Jiang, Q.Y. Luo, J.D. Ding, Hybrid interpenetrating network of polyester coronary stent with tunable biodegradation and mechanical properties, Biomaterials 304 (2024) 122411.

[76] Y. Gao, Q.M. Ma, Bacterial infection microenvironment-responsive porous microspheres by microfluidics for promoting anti-infective therapy, Smart Med 1 (1) (2022) e20220012.

[77] X.Y. Cao, L.Y. Sun, Z.Q. Luo, X. Lin, Y.J. Zhao, Aquaculture derived hybrid skin patches for wound healing, Eng. Regen. 4 (1) (2023) 28–35.

[78] G. Wang, C.Y. Gao, B.H. Xiao, J. Zhang, X.Y. Jiang, Q.S. Wang, J.Z. Guo, D. Y. Zhang, J.X. Liu, Y.H. Xie, C. Shu, J.D. Ding, Research and clinical translation of trilayer stent-graft of expanded polytetrafluoroethylene for interventional treatment of aortic dissection, Regen. Biomater. 9 (2022) rbac049.

[79] P.G. Wang, M. Xian, X.P. Tang, X.J. Wu, Z. Wen, T.W. Cai, A.J. Janczuk, Nitric oxide donors: chemical activities and biological applications, Chem. Rev. 102 (4) (2002) 1091–1134.

[80] X.H. Li, S.K. He, B.Y. Ma, Autophagy and autophagy-related proteins in cancer, Mol. Cancer 19 (1) (2020) 12.

[81] B.W. Yang, L. Ding, H.L. Yao, Y. Chen, J.L. Shi, A metal-organic framework (MOF) Fenton nanoagent-enabled nanocatalytic cancer therapy in synergy with autophagy inhibition, Adv. Mater. 32 (12) (2020) 1907152.

[82] E. Aygören-Pürsün, A. Zanichelli, D.M. Cohn, M. Cancian, R. Hakl, T. Kinaciyan, M. Magerl, I. Martinez-Saguer, M. Stobiecki, H. Farkas, S. Kiani-Alikhan, V. Grivcheva-Panovska, J.A. Bernstein, H.H. Li, H.J. Longhurst, P.K. Audhya, M. D. Smith, C.M. Yea, A. Maetzel, D.K. Lee, E.P. Feener, R. Gower, W.R. Lumry, A. Banerji, M.A. Riedl, M. Maurer, An investigational oral plasma kallikrein inhibitor for on-demand treatment of hereditary angioedema: a two-part, randomised, double-blind, placebo-controlled, crossover phase 2 trial, Lancet 401 (10375) (2023) 458–469.

[83] S.G. Kathman, S.J. Koo, G.L. Lindsey, H.L. Her, S.M. Blue, H. Li, S. Jaensch, J. R. Remsberg, K. Ahn, G.W. Yeo, B. Ghosh, B.F. Cravatt, Remodeling oncogenic transcriptomes by small molecules targeting NONO, Nat. Chem. Biol. 19 (2023) 825–836.

[84] A. Zorba, C. Nguyen, Y. Xu, J. Starr, K. Borzilleri, J. Smith, H. Zhu, K.A. Farley, W. D. Ding, J. Schiemer, X.D. Feng, J.S. Chang, D.P. Uccello, J.A. Young, C.N. Garcia-Irrizary, L. Czabaniuk, B. Schuff, R. Oliver, J. Montgomery, M.M. Hayward, J. Coe, J. Chen, M. Niosi, S. Luthra, J.C. Shah, A. El-Kattan, X.Y. Qiu, G.M. West, M.C. Noe, V. Shanmugasundaram, A.M. Gilbert, M.F. Brown, M.F. Calabrese, Delineating the role of cooperativity in the design of potent PROTACs for BTK, P. Natl. Acad. Sci. 115 (31) (2018) E7285–E7292.

[85] W.Y. Hua, J. Zhao, X.Y. Wang, S.N. Pei, S.H. Gou, A lysosome specific theranostic NO donor inhibits cancer cells by stimuli responsive molecular self-decomposition with an on-demand fluorescence pattern, Analyst 144 (22) (2019) 6681–6688.

[86] H.J. Zhang, X. Li, Z.H. Qu, W.Q. Zhang, Q.S. Wang, D.L.G. Cao, Y.B. Wang, X. Wang, Y. Wang, L. Yu, J.D. Ding, Effects of serum proteins on corrosion rates and product bioabsorbability of biodegradable metals, Regen. Biomater. (2023) rbad112.

[87] S.A. duPre, K.W. Hunter, Murine mammary carcinoma 4T1 induces a leukemoid reaction with splenomegaly: association with tumor-derived growth factors, Exp. Mol. Pathol. 82 (1) (2007) 12–24.

[88] Y. Zhang, X.Y. Wang, C.C. Chu, Z.J. Zhou, B.Q. Chen, X. Pang, G. Lin, H.R. Lin, Y. X. Guo, E. Ren, P. Lv, Y.S. Shi, Q.B. Zheng, X.H. Yan, X.Y. Chen, G. Liu, Genetically engineered magnetic nanocages for cancer magneto-catalytic theranostics, Nat. Commun. 11 (1) (2020) 5421.